

Mixing and turbulent fluxes in the metalimnion of a stratified lake

Angelo Saggio¹

Department of Ecology and Evolutionary Biology, Federal University of São Carlos, São Carlos, SP 13565-905, Brazil

Jörg Imberger

Department of Environmental Engineering, Centre for Water Research, The University of Western Australia, Nedlands, Western Australia 6907, Australia

Abstract

Turbulent mixing within the metalimnion of a stratified lake was investigated using a portable flux profiler (PFP) capable of resolving all three components of the velocities, the conductivity, and the temperature microstructure. Presented is a detailed description of the techniques used in the data processing, particularly in the separation of the turbulence from the internal wave signal. The sampling, carried out in Lake Kinneret (Israel) during the summer for 3 consecutive years, showed that most of the time the vertical flux through the metalimnion was negligible, but, at times, the eddy diffusivity did reach values as high as $10^{-2} \text{ m}^2 \text{ s}^{-1}$. A comparison between direct measurement of the vertical fluxes obtained from the PFP data with that from indirect estimates of the fluxes shows good agreement for the $6 \leq Fr_\gamma < 100$ range. Scaling of the turbulence based on Fr_γ and Ri reveal two classes of turbulent regimes: (1) due to traumata characteristic of internal wave-wave interaction and, another, (2) more energetic and due to shear-driven turbulence. The PFP penetrated the water relatively slowly (0.1 m s^{-1}) allowing the measurement of temperature fluctuations down to 1 mm and, at the same time, also providing information of the velocity fluctuations. This is different from previous oceanographic measurements, which are always gathered with instrument traversing the water column at velocities closer to 1 m s^{-1} , preventing regime (1) from being detected.

The vertical exchange between the surface and deep waters in stratified lakes is a central issue in the understanding of the fluxes of particles and nutrients and, consequently, the eutrophication in these water bodies. Imberger (1998) drew a conceptual model of these flux paths in a stratified lake where the wind induces mixing in the surface layer and energizes basin scale internal waves that, in turn, distribute this energy around the lake, leading to mixing mainly near the boundaries (Gloor et al. 1994; Lemckert and Imberger 1998) and reduced fluxes through the metalimnion in the interior of the lake.

Even though the vertical fluxes in the metalimnion are small, their quantification is essential for the interpretation of observed biological and chemical parameter variations (Nishri et al. 2000). Naturally, two questions arise as we approach the mixing in the metalimnion: first, what is the magnitude and, second, what are the mechanisms energizing the mixing. Direct measurements of the buoyancy fluxes carried out in the ocean (Moum 1990, 1996a; Yamazaki and Osborn 1993) show the difficulties in making these measurements and provide the first comparison between the direct determination of the fluxes with the more easily ob-

tained indirect estimates (Osborn and Cox 1972; Osborn 1980). Basically, the direct measurements show the occurrence of both down-gradient and up-gradient fluxes in the thermocline of these water bodies, leading to a small net down-gradient flux. This oscillation in the sign of the fluxes was partially attributed to the short length of the data records but mainly caused by the intermittent nature of the events. Most of the experiments also show that the indirect estimates overestimate the vertical fluxes in the thermocline by either accounting only for the down-gradient fluxes or disregarding the time dependency of the turbulence (Gargett and Moum 1995). The nature of the mixing events has been investigated by Peters et al. (1994, 1995b). They found in the Pacific equatorial undercurrent that the large-scale shear alone was a poor predictor of the mixing, but the observed variations in turbulent mixing were associated with variations of fine-scale shear. The creation of turbulence by shear instabilities was consistent with the observations with transient fine-scale processes, such as internal waves, providing the bulk of the shear.

In the present paper we investigate the mixing in the metalimnion of stratified lakes by combining measurements of the background flow conditions with measurements of properties of the turbulence, including direct measurement of the buoyancy fluxes and Reynolds stresses. The paper is primarily concerned with revealing the properties and nature of the turbulence associated with mixing in the metalimnion but also quantifies the vertical fluxes. A detailed methodology describing our procedure to extract the turbulent fluctuations from the measured signals and compute the fluxes is presented in Methodology. The occurrence of turbulent patches in the metalimnion presents the background conditions in the

¹ Corresponding author (saggio@iris.ufscar.br).

Acknowledgments

The authors wish to thank Tamar Zohary and the Lake Kinneret Laboratory (KLL) for the very considerable technical and logistic support and Werner Eckert for coordinating the field experiments with K.L.L. Sheree Feaver managed all the field logistics for CEFD, and her help is gratefully acknowledged. This project was supported by the Centre for Environmental Fluid Dynamics. This paper forms Centre for Water Research reference ED 1252-AS.

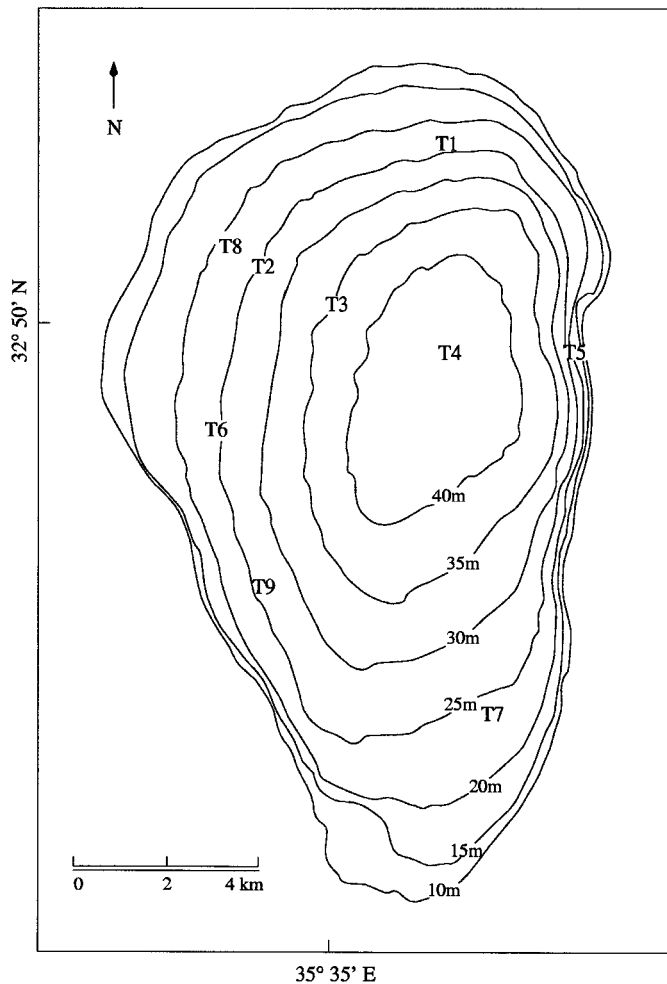


Fig. 1. Map of Lake Kinneret and location of sampling stations.

lake, describes a typical mixing event, and shows the distribution of these events. In properties of the turbulence within a turbulent patch all the microstructure data collected is presented and the vertical fluxes are estimated from direct and indirect measurements. In scaling of the turbulence properties a scaling of the turbulence is introduced and the nature of the turbulent events is discussed. The conclusions are presented at the end.

The field measurements were carried out in Lake Kinneret (Fig. 1) during the summer for 3 consecutive years (1997, 1998, and 1999). In each case, the turbulence experiments were accompanied by an internal wave experiment (Antenucci et al. 2000), a benthic boundary layer experiment (Lemckert and Imberger 1998), and a series of limnological studies (Nishri et al. 2000).

Methodology

Microstructure profiles of temperature, temperature gradient, conductivity, and velocity were measured with the portable flux profiler (PFP; Imberger and Head 1994). The PFP has two combined four-electrode conductivity and tem-

perature sensors mounted in the front of the probe between a pair of two-component laser Doppler velocimeters (LDV). Arranged in this way, the probe was able to sample at 100 Hz an average volume of 8 mm³ as it free fell through the water column with an almost constant speed of 0.1 m s⁻¹. The temperature and conductivity sensors had a resolution of 0.001°C and 0.0004 S m⁻¹, and each LDV system was able to measure the vertical and one horizontal component of the velocity with a resolution of 0.001 m s⁻¹. The pair of LDV systems were mounted orthogonally in the probe, allowing us to measure all three components of the velocity field with two independent estimates of the vertical velocity. The probe was also equipped with a compass, tilt, and pressure sensors with resolutions of 1.4°, 0.25°, and 0.003 m, respectively. Each profile thus yielded a set of temperature, conductivity, and velocity microstructure from which it was possible to derive turbulent fluctuations of these quantities as well as the mean velocity, the background shear, and the Richardson number profiles. In the 1999 experiment, the probe had only one pair of fast response temperature and conductivity sensors, and the previous analogue electronics of this system were replaced with digital electronics.

The data processing basically consisted of (1) calculation of the horizontal velocity of the vehicle, flow velocities, and shear; (2) calculation of temperature, density, and velocity fluctuations and turbulent length scales; (3) segmentation of the profiles into patches of stationary signal; and, finally, (4) estimation of the properties of the turbulence within patches in the metalimnion.

The density was calculated from the temperature and conductivity signals that were previously digitally sharpened and smoothed (Fozdar et al. 1985). The absolute water velocity in the horizontal was computed as the measured velocity (velocity relative to the probe) plus the probe motion. The horizontal motion of the probe was calculated by estimating the drag on the probe (Hendricks and Rodenbusch 1981) and then solving the horizontal momentum equation as the instrument moved vertically through the water column. First, the measured horizontal velocities, relative to the probe, were low-pass filtered at 0.40 Hz and then decomposed into their north-south and west-east components. These filtered velocities relative to the probe were used to compute the drag $dF_i = 0.5 \rho_i C (A_u u_i |u_i| + A_w u_i w_i)$ at every point of the profile where ρ_i is the density, C is a calibrated coefficient equivalent to $C_d/(1 + C_m)$ where C_d is the drag coefficient and C_m is the added mass coefficient, A_u and A_w are the area projections of the vehicle in the horizontal and vertical directions, and u_i and w_i are the velocity components in the horizontal and in the vertical, respectively. The absolute water velocity was calculated using $U_{i+1} = u_i + U_i + dF_i \Delta t M^{-1}$, where $i + 1$ and i are two consecutive points in the profile, Δt is the sampling interval, and M is the mass of the probe (~39 kg). This procedure was followed for the north-south and west-east directions independently (U and V velocity components, respectively), and the bottom was used as a reference point where the probe was assumed to be stationary. The thin (2-mm diameter) umbilical cable exerted only a negligible drag on the vehicle as the profile depth was short (less than 40 m), and the water velocities were generally confined to a thin layer in the metalimnion.

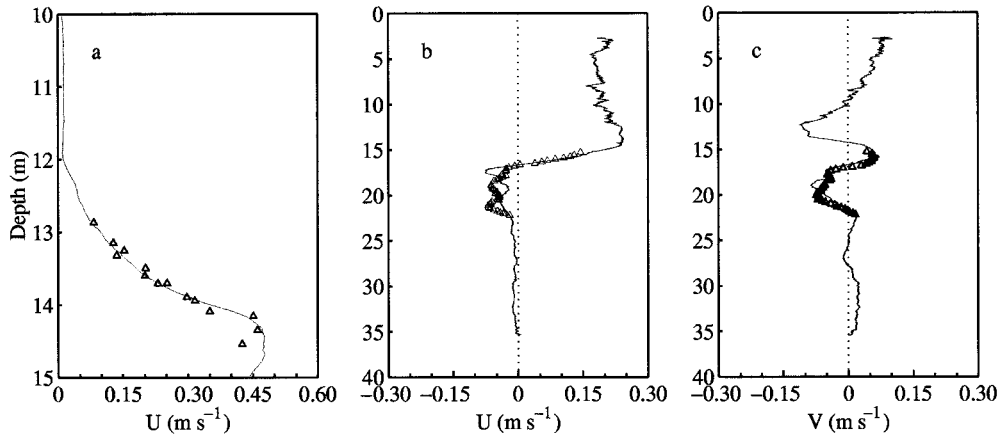


Fig. 2. Comparison between velocity profiles estimated with the PFP (solid line) and independent measurements (triangles). (a) Velocity profiles measured with an electromagnetic current meter ECM and the PFP in Lake Ogowara (Japan). (b) and (c) Velocity profiles measured in Lake Kinneret with the PFP and a pair of acoustic Doppler current profilers (ADCP), south–north and east–west velocity components, respectively. In both field experiments the coefficient C was 0.35, yielding good agreement between the measurements. In Lake Ogowara, owing to strong currents close to the bottom bed, the approximation that the probe remains still when reaching the bottom did not hold and a S4 current meter was used as a reference point for the velocity calculation.

The coefficient C was calibrated against velocity profiles measured with an electromagnetic current meter (ECM) and an acoustic Doppler current profiler array (ADCP) in two lakes under very different flow conditions (Fig. 2). In general, comparison was excellent, especially for length scales larger than 1 m. The PFP revealed small velocity variations at smaller scales (Fig. 2b,c) that could not be reproduced by the in situ acoustic profiler because its time resolution was 15 min. However, given the large mass of the PFP (39 kg) and its length (2 m), the motion of the probe contributed little to such small-scale (≤ 1 m) velocity variations, and it can be safely assumed that the PFP correctly measured the smaller scale motions. The probe was also very stable in the metalimnion, with the largest tilt oscillation recorded being around 2° over 1 m, which gives negligible contribution to the velocity measurements due to the proximity of the center of gravity of the probe and the sensors (~ 0.50 m). The quality indicators from the two laser Doppler systems consistently verified that the velocity estimates had high statistical confidence.

The velocity shear squared $S^2 = (\partial U/\partial z)^2 + (\partial V/\partial z)^2$, the buoyancy frequency squared $N^2 = -(g/\rho_o)(\partial \bar{\rho}/\partial z)$ (using the sorted density profile, $\bar{\rho}$), and the gradient Richardson number $Ri = N^2/S^2$ were computed from signals low-pass filtered at 0.4 Hz, equivalent to a vertical scale of approximately 0.25 m.

The following steps in the data processing yielded estimates of the vertical length scales and the turbulent fluctuations of the variables. The density fluctuation ρ' , temperature fluctuation θ' , and displacement scale L_d were obtained by comparison between the measured and the sorted density profiles (Thorpe 1977). The centered displacement scale, L_c , which is an estimate of the displacement scale positioned at the center of the overturns, was calculated by (1) moving L_d by half of its value along the profile, (2) accumulating the absolute values of these re-

positioned L_d and, finally, (3) taking the average of these values. A graphical explanation of the procedure can be found in Imberger and Boashash (1986). An envelope function of L_c was then computed and used as a scale for a variable length filter employed in the calculation of the velocity turbulent fluctuations. The envelope was defined as the maximum of L_c over a window of length L_c , this window having a variable size adjusted as the magnitude of L_c changed in the profile. The envelope was calculated at each point i of the profile as $\hat{L}_{ci} = \max[L_{cj}]$, with $j \in [i - W_i/2; i + W_i/2]$. The window W_i was defined as $W_i = \hat{L}_{c(i-1)} \Delta t^{-1} D_i^{-1}$, where Δt is the sampling interval and D_i is the probe drop velocity at point i . The envelope was calculated from both directions of the signal and then averaged. This definition of the envelope function meant that the value of L_c was used as the scale separating the turbulent and mean signals (Peters et al. 1995a). In practice, we multiplied the envelope function by 2 to avoid removing a fraction of the signal at the scale of L_c to compensate for a lack of sharpness of the filter. The maximum value of the envelope was limited to 2 m, the length of the probe. The filter applied to the velocity signals was a non-recursive Gaussian filter with standard deviation equal to the value of the envelope function at each point of the profile. The velocity fluctuations were calculated as the difference between the measured and the filtered signals; Fig. 3 shows an example of raw and fluctuation signals using this procedure. This filtering technique produced good results and generated profiles of ρ' very similar to the ones obtained from the difference between the recorded and reordered profiles (Fig. 4). The nonrecursive nature of the filter and the use of variable lengths based on L_c avoided problems such as rippling and phase shifting even at abrupt steps such as found at the top of the benthic boundary layer.

Segments of statistically stationary signal within the pro-

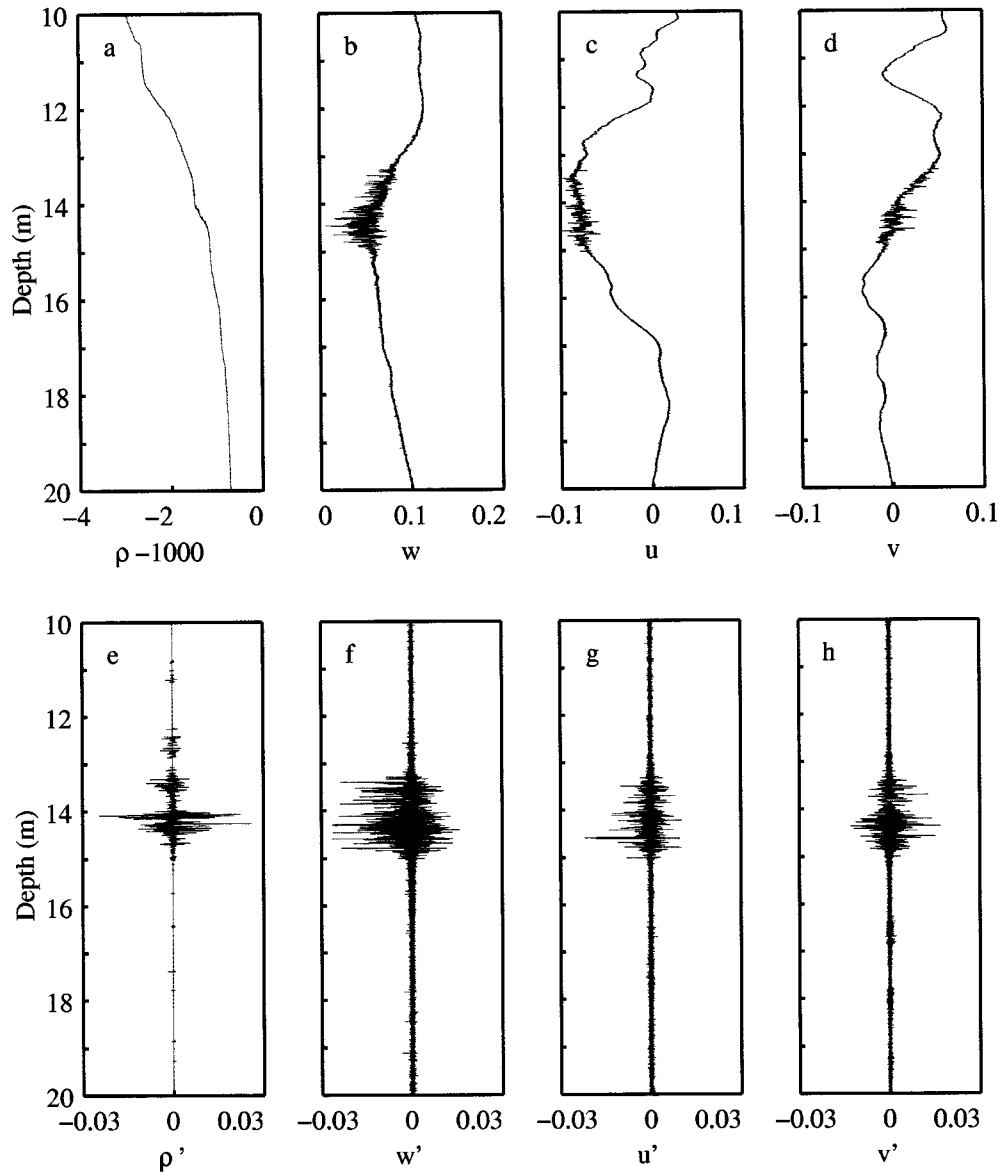


Fig. 3. Example profile from Lake Kinneret showing a turbulent patch in the thermocline. (a) Density ρ , (b) vertical velocity w , (c) north-south velocity component u , and (d) west-east velocity component v measured by the PFP and their calculated fluctuations (e) ρ' , (f) w' , (g) u' , and (h) v' are shown in the figure. The fluctuations were obtained from the difference between the measured signal and a low-pass filtered signal using a Gaussian filter of variable length based on the displacement scale L_c . The velocities have units of m s^{-1} and the density of kg m^{-3} .

files were determined with a segmentation algorithm applied to the temperature gradient signal. This procedure is based on the comparison of the spectra of two adjacent windows that are slid along the signal; a detailed description of the procedure is given in Imberger and Ivey (1991). The results presented in the paper are derived from the statistics and spectral properties of these segments, which were always longer than $3 L_c$, having in average length greater than $20 L_c$.

The correlations $\overline{w'\rho'}$, $\overline{w'u'}$, $\overline{w'v'}$ and variances w'^2 , u'^2 , and v'^2 were calculated from the integration of their cospectra (autospectra for variances) from the minimum frequency

corresponding to the scale L_c in the segment to 32 Hz, the frequency correspondent to the start of the blue noise in the velocity estimates. The white noise level in each velocity component was determined from calm portions of the profiles and was subtracted from the autospectra prior to their integration. The variable filter based on L_c was an effective mean of detrending the signals before the spectra calculation, and, in the cases where the signals were much stronger than the noise levels, the integration of the spectra as described above produced the same result as the mean of the product of the signal fluctuations within the segments. Since we had two independent measurements of the vertical velocity (w'_1

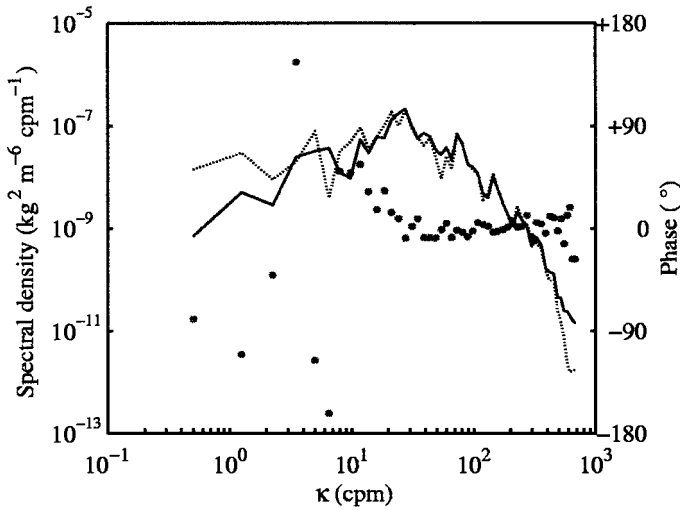


Fig. 4. Spectra of the density fluctuations ρ' obtained from the monotizing technique (solid line) and from a variable length filtering procedure (dotted line). The phase difference between the signals is given by the full circles. The displacement scale L_T for this turbulent patch was 0.019 m (≈ 50 cpm), and it is shown in the figure that for scales shorter than this length the spectra are identical and the phase difference is zero. The spectra and phase correspond to the segment between 13 and 15 m depth shown in Fig. 3.

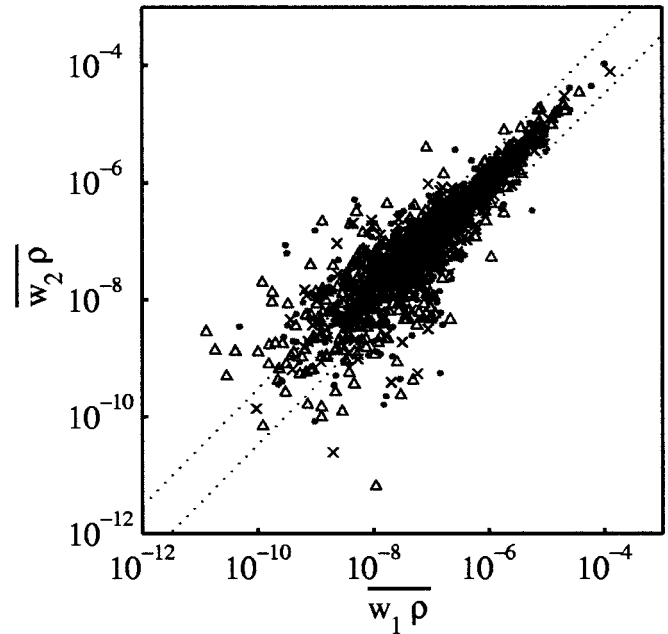


Fig. 5. Two independent measurements of the vertical velocity (w'_1 and w'_2) are obtained with the PFP, each one for a pair of LDV system, allowing a comparison between direct estimates of the vertical fluxes. In the log-log plot all the data points that had $w'_1\rho'$ and $w'_2\rho'$ of the same sign are shown; when both fluxes were negative the absolute value was taken before plotting. About 20% of the original data set is not shown in the plot because the fluxes had the opposite sign. The measurements show good agreement distributing along a 45° slope, and the increase in scatter as the fluxes reduces is mostly associated with very small fluctuations in velocity. To increase confidence in the results, we work in the next sections of the paper only with the data points between the dotted lines in the plot, corresponding to $\frac{1}{3} < w'_1\rho'/w'_2\rho' < 3$. This figure has the data collected in 1997 (triangles), 1998 (dots), and 1999 (crosses) field experiments.

and w'_2) given by each pair of LDV, we could also compare $w'_1\rho'$ and $w'_2\rho'$, excluding all the data with ratio $w'_1\rho'/w'_2\rho'$ smaller than $\frac{1}{3}$ or larger than 3 increasing the confidence in the results (Fig. 5).

The rate of dissipation of turbulent kinetic energy was estimated from the velocity signal, shear dissipation ϵ_s , and from the temperature microstructure, Batchelor dissipation ϵ_B . The shear dissipation was calculated similarly to Piccirillo and Van Atta (1997) using the three measured velocity strains as $\epsilon_s = [5(\partial w'/\partial z)^2 + 5/2(\partial u'/\partial z)^2 + 5/2(\partial v'/\partial z)^2]\nu$, where ν is the kinematic viscosity and the averages were obtained in the wavenumber domain in a similar way to the correlations described in the previous paragraph. The Batchelor dissipation was calculated by fitting a Batchelor spectrum to the temperature gradient signal (Luketina 1987) and followed by visual inspection of the raw and fitted Batchelor spectra; unclear fits were discarded. Segments with dissipation less than $10^{-10} \text{ m}^2 \text{ s}^{-3}$ were also discarded because they originated from segments where the temperature signal was below the threshold of the thermistor's resolution. A detailed description of the fitting procedure and examples of typical spectra are presented in Luketina and Imberger (2000). The shear and the Batchelor dissipations show good agreement at values higher than $10^{-7} \text{ m}^2 \text{ s}^{-3}$; however, below this level, the scatter increases and on average ϵ_s becomes a quarter of ϵ_B (Fig. 6). The increase in scatter at low values of dissipation may be expected because these data involve very small fluctuations in the velocity. The systematic lower estimate of ϵ_s is most likely due to the different assumptions of isotropy underlying the two methods, as also observed by Itsweire et al. (1993) when compared to different estimates of dissipation using results of direct numerical simulations.

Since the difference between ϵ_B and ϵ_s was small compared to their range of variation, both were considered reasonable estimates of the rate of dissipation. In this paper we adopt the Batchelor dissipation (hereafter just signed as ϵ) as a measure of the rate of dissipation of turbulent kinetic energy because this method is the more common in lake measurements. The Cox number, C , was obtained from the integration in wavenumber space of the fitted Batchelor spectra, which guaranteed the separation of the turbulent contribution from the fine-scale contamination (Luketina and Imberger 2000).

The statistics used to derive properties of the segment were (1) median of the buoyancy frequency N^2 , the velocity shear S^2 , and the gradient Richardson number Ri , (2) root mean square (rms) of the Thorpe displacement scale $L_T = \text{rms}(L_d)$, (3) skewness of L_c , and (4) sparseness of L_c —percentage of points with nonzero displacement scales. Medians were used instead of arithmetic means as the mentioned variables did not have Gaussian distribution within the segments. In the calculation of L_T , only points with nonzero displacement were accounted since, as will be discussed later in the paper, a large number of segments with good Batchelor spectra but with very few overturns within the

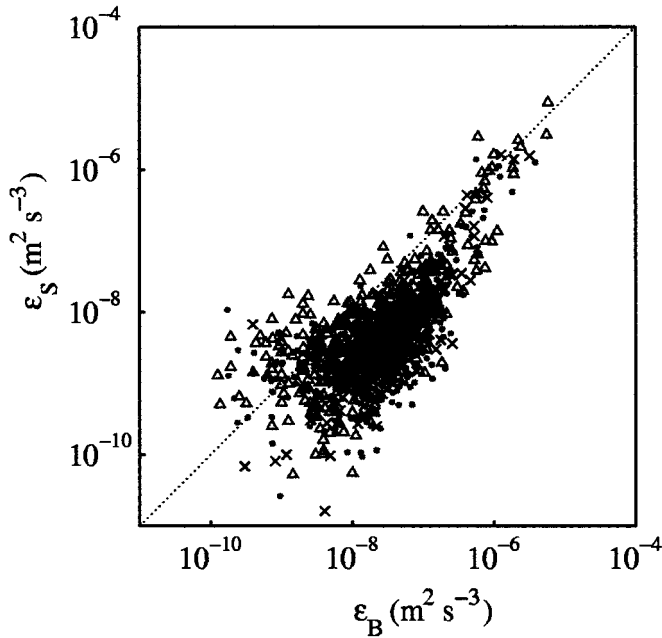


Fig. 6. Comparison between estimates of the rate of dissipation of turbulent kinetic energy. The dissipation ϵ_B was obtained through fitting of the Batchelor spectrum as described in Luketina and Imberger (2000) and ϵ_S was calculated from three velocity strains as $[5(\partial w'/\partial z)^2 + 5/2(\partial u'/\partial z)^2 + 5/2(\partial v'/\partial z)^2]\nu$ (Piccirillo 1993). The data collected in 1997 are shown as triangles, in 1998 as dots, and in 1999 as crosses.

segments were observed. We adopted L_T as a measure of the overturns in the segments for consistency with the literature and because of its equivalence to the mean value of L_c . The centered displacement scale L_c was mainly used as scale for the separation of the turbulent and nonturbulent signals (through the variable filter) and to describe the distribution of the overturns inside the segments (through its skewness and sparseness). The velocity scale q was calculated as $(w'^2 + u'^2 + v'^2)^{1/2}$, and the Batchelor dissipation was used as an estimate of the rate of dissipation of turbulent kinetic energy ϵ . With the properties of the segments described as above, three dimensionless numbers of fundamental importance in the description of the turbulence were calculated: the turbulent Reynolds number $Re_t = qL_T\nu^{-1}$, the turbulent Froude number $Fr_t = qL_T^{-1}N^{-1}$, and the strain ratio $Fr_\gamma = \epsilon^{1/2}\nu^{-1/2}N^{-1}$ (Ivey and Imberger 1991).

The selection of segments in the metalimnion was done by visual inspection of the whole temperature profile. Segments with poor Batchelor spectral fits, dissipation below the threshold, the overturn length scale less than 0.001 m, or a buoyancy flux that differed by more than a factor of 3 between the two redundant sensors were all excluded.

The occurrence of turbulent patches in the metalimnion

The background internal wave activity—A daily westerly wind blows over Lake Kinneret during the summer, exciting an extensive set of internal waves resulting in vertical isotherm displacements as high as 10 m (Fig. 7). Like the wind, the isotherm displacement shows a daily pattern with the

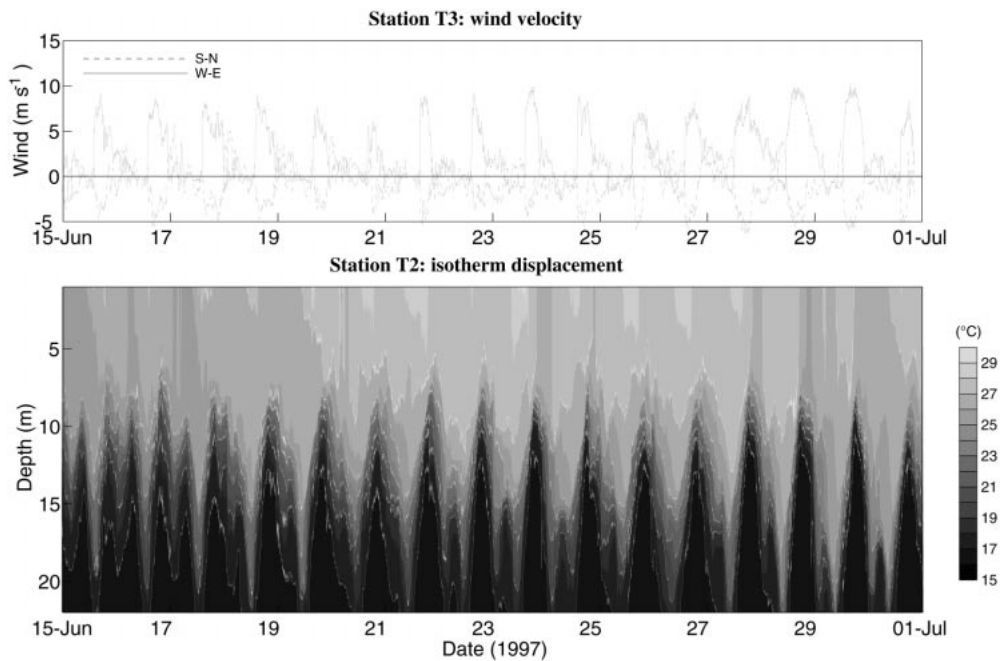


Fig. 7. Output from thermistor chain at Sta. T2 during the 1997 Lake Kinneret experiment: (a) wind velocity and (b) isotherm displacements. The contour lines limit 2°C intervals for the temperatures indicated close to the colorbar. The original 20-s sampling interval records were filtered and decimated to give a 5-min interval output.

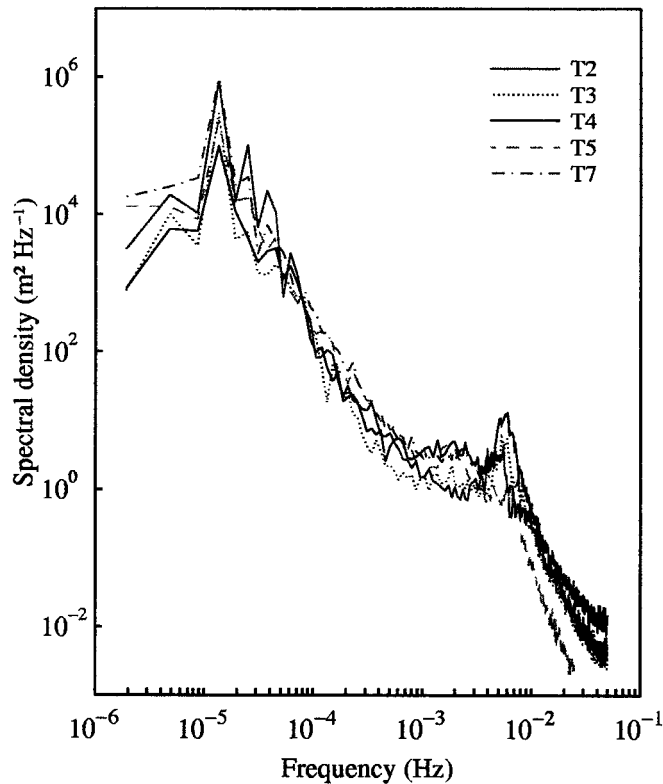


Fig. 8. Spectral density of the vertical displacement of isotherm 20°C at several stations around the lake during the 16-d period shown in Fig. 7. The most energetic peak in the spectra occurred at 1.1×10^{-5} Hz (1 d), matching the large amplitude wave observed in the isotherm record (Fig. 7). A second frequency peak at 2.3×10^{-5} Hz was stronger in the stations around the lake than in the interior, corresponding to the 12 hours period wave in the isotherm record. These two frequency peaks correspond to the largest observed waves in the signal and were identified as a Kelvin and Poincaré type waves through the coherence between the stations and velocity measurements (Antenucci et al. 2000).

magnitude of the vertical displacement determined by the phase difference between 24- and 12-h period waves and the strength of the previous day's wind impulse (Antenucci et al. 2000). The predominant waves energized by this oscillatory forcing were a 24-h period Kelvin wave, 12-h period Poincaré waves, and forced seiches (Fig. 8), which were identified by coherence between eight thermistor chains stations around the lake and velocity measurements (Lemckert and Imberger 1998; Antenucci et al. 2000). Whereas the Kelvin waves generate high velocities at the bottom bed around the lake by sweeping over the slopes, the Poincaré waves and forced seiches produce regions of strong shear in the interior. The present paper focuses exclusively on the turbulence in the interior of the lake at the level of the metalimnion, where the shear and high-frequency wave activity is the most intense.

By way of illustration, we shall first consider the development of the mean shear accompanying the results from a set of turbulence measurements conducted between 2300 h (local time: GMT-3, summer time) and 0500 h on 23 June 1997 at the center of the lake at Sta. T4 (Fig. 1). These

measurements are typical and highlight the evolution of the turbulent mixing in the metalimnion under the intense internal wave activity. During this time the wind conditions were calm and Sta. T4 was experiencing strong shear due to the evolution of the 12-h period Poincaré wave.

The day prior to these measurements, 22 June, was a typical day with wind speeds below 2 m s^{-1} until 1400 h, at which time the westerly daily winds commenced and shortly after reached speeds between 8 and 10 m s^{-1} . The wind halted in the evening, and conditions returned to calm with winds lower than 2 m s^{-1} by about 2030 h. The wind remained low until the next day, when the same wind pattern repeated. The temperature structure prevailing during the night of the measurement period is shown in Fig. 9a. The water column was strongly thermally stratified with epilimnion temperatures of about 28°C and hypolimnion temperatures of about 16°C ; a sharp metalimnion at around 13-m depth separated the epilimnion and hypolimnion until about 0330 h, at which time a noticeable opening and deepening of the isotherms occurred. The water speed (Fig. 9c) and direction (Fig. 9d) reflected the metalimnion behavior during the observation period. Initially, between 2300 and 0330 h, the velocity field was characterized by a strong shear across a 2-m thick layer located at depth of 13 m; during this period the water in the epilimnion was flowing north with an initial velocity (at 2300 h) greater than 0.3 m s^{-1} but then reducing through the night. The period between 2300 and 0330 h covers the stage of the 12-h wave evolution when the thermocline was almost horizontal across the lake and the shear was maximum at the center of the lake following the release of the thermocline by the wind by about $\frac{1}{4}$ of the period of the wave (approximately 3 h after the wind stopped at 2030 h).

By 0330 h the surface water velocities had reduced to less than 0.15 m s^{-1} and a second flow pattern consisting of a jetlike structure flowing west within the metalimnion was observed. This intrusion, or mode two wave, caused the shear in the metalimnion to decrease, leading to an increase in the gradient Richardson number (Fig. 9b) from less than 0.5 (2300 to 0300 h) to greater than 0.5 (0300 to 0500 h). During the entire period of measurement, the flow near the lake bottom was characterized by very low Richardson numbers, indicating the presence of a turbulent benthic boundary layer as discussed Nishri et al. (2000).

The conditions described above were the result of the interaction of a 12-h period vertical mode one and a 20-h period vertical mode two Poincaré waves induced by the momentum introduced with the wind pulse (Münnich et al. 1992; Antenucci et al. 2000). These long periodic waves have time scales of several hours and so present pseudo-steady stratified shear flow conditions in which the turbulence may evolve as in a steady shear flow (Rohr et al. 1988a,b).

A typical turbulent event—The results of the various properties of the turbulence at Sta. T4 during the above time period are shown in Fig. 10a–i. The rate of dissipation of turbulent kinetic energy ϵ was mostly greater than $10^{-9} \text{ m}^2 \text{ s}^{-3}$ over the whole metalimnion (Fig. 10a), above the threshold for the measurement technique (10^{-10} m^2

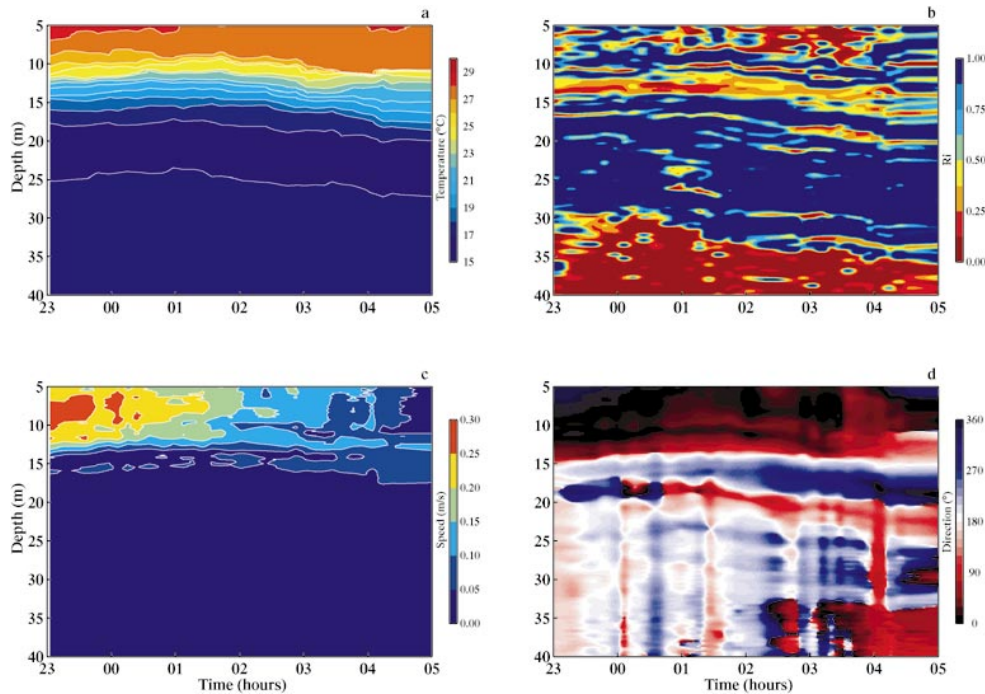


Fig. 9. (a) Temperature, (b) Richardson number, (c) speed, and (d) direction during the night experiment on 22 June 1997 at Sta. T4.

s^{-3}), indicating that the whole metalimnion exhibited a definite measurable turbulent signature. Three distinct layers may be identified from the data set collected over this period: (1) the lower metalimnion between 18- and 15-m depth (temperatures from 17 to 18.5°C), (2) the central metalimnion (hereafter referred as the thermocline) between 15- and 13-m depth (18.5 to 21°C), and (3) the water above 13-m depth, the upper metalimnion (temperatures above 21°C). The turbulence intensity in the lower metalimnion was consistently weak, with values of dissipation between 10^{-9} and 10^{-8} $m^2 s^{-3}$. In the thermocline, dissipation values were generally elevated and in excess of 10^{-6} $m^2 s^{-3}$, whereas in the upper metalimnion dissipation values were more variable and ranged between 10^{-9} $m^2 s^{-3}$ and 10^{-6} $m^2 s^{-3}$.

Consider first the lower metalimnion where the gradient Richardson number was generally larger than 0.5 (Figs. 9b and 10b). The turbulent properties in this region showed small variance, with average values of the Thorpe displacement scale L_T being around 0.01 m (Fig. 10c). The buoyancy flux and shear production in the kinetic energy budget were insignificant in this layer (Fig. 10d–f), the turbulent Froude number Fr , was less than 1, the turbulent Reynolds number Re , was smaller than 10, and the strain ratio Fr_γ ranged between 1 and 3 (Fig. 10g–i). The turbulence in the lower metalimnion was thus characterized by low strain ratios and very small-scale overturns, indicating that the turbulence was possibly energized by wave–wave interaction as suggested by Teoh et al. (1997).

The thermocline layer located immediately above the lower metalimnion was characterized by gradient Richardson numbers consistently less than 0.5. This lower stability led

to turbulence that was more energetic ($10^{-9} < \epsilon < 10^{-5}$ $m^2 s^{-3}$), that had larger displacement scales (average of $L_T > 0.02$ m) and markedly elevated buoyancy fluxes (Fig. 10d), and that was energized by shear production (Fig. 10e–f). The turbulent Froude number (average larger than 1; Fig. 10g), turbulent Reynolds number (average larger than 10; Fig. 10h), and the strain ratio (average larger than 5; Fig. 10i) indicate that the turbulence in this region was energetic with convection playing a minor role, especially at the smaller scales.

In the upper metalimnion, the value of the gradient Richardson number fluctuated widely from cast to cast from 0.1 to over 2.0. It is therefore not surprising that the turbulent properties of the segments in this region showed an equally wide scatter, but it should be pointed out that the buoyancy and momentum fluxes showed consistently low values.

Frequency of occurrence of turbulent patches—During the 1997, 1998, and 1999 summer experiments several stations around the lake were sampled at different times, producing a total of 698 microstructure profiles. These profiles were processed as described in Methodology, yielding approximately 1,100 turbulent segments in the metalimnion. On average, 35% of the metalimnion was covered by turbulent segments (Fig. 11). When interpreting the results of the next sections it is thus important to remember that much of the metalimnion much of the time was laminar or close to laminar.

Distribution of the dissipation over events—Of the segments chosen as representing turbulent flow, 95% had a buoyancy frequency N between 10^{-2} and 10^{-1} s^{-1} , but the

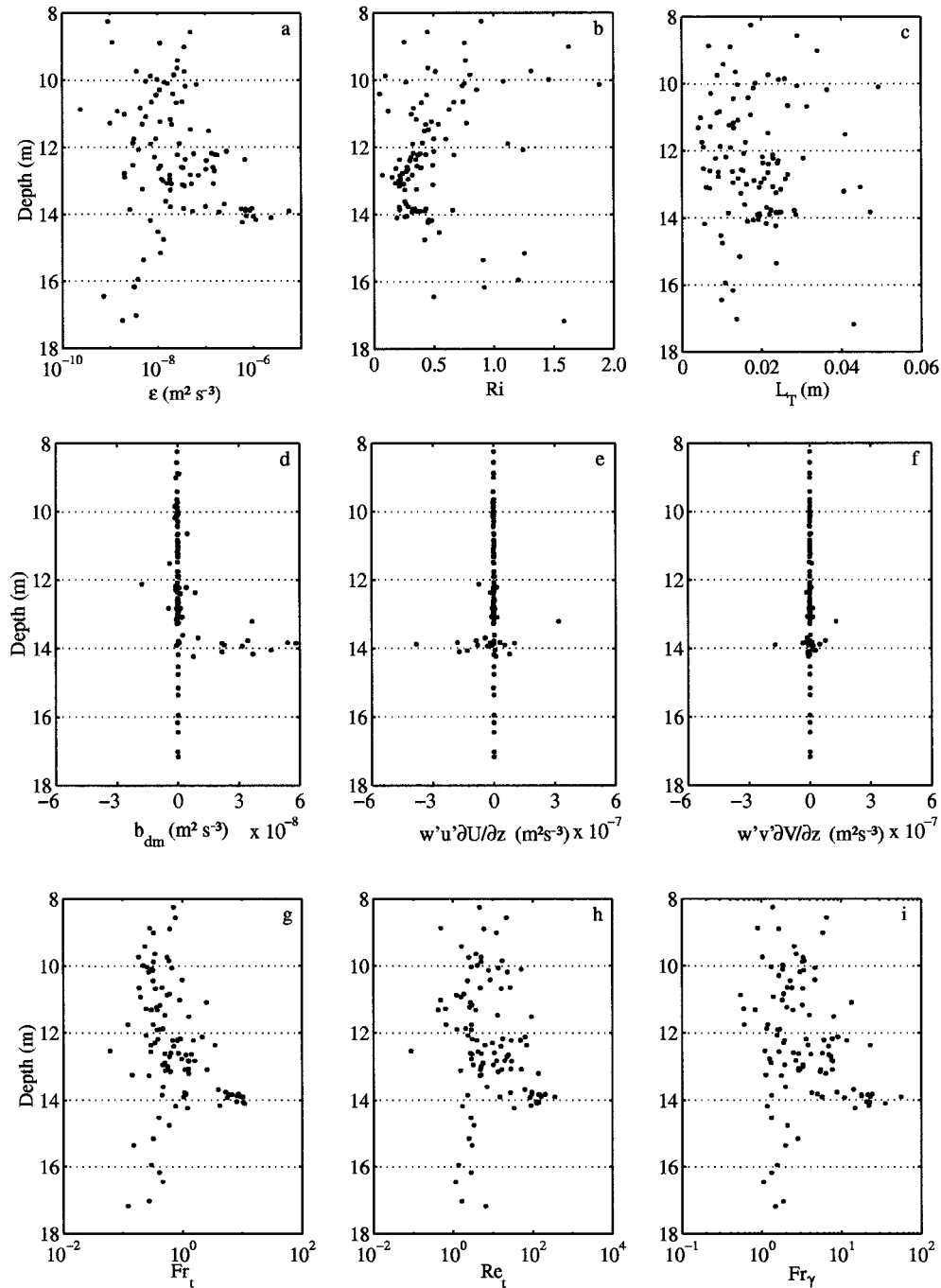


Fig. 10. Turbulent properties in the metalimnion from 25 profiles collected during the period of high shear between 2300 and 0330 h on 22 June 1997 at Sta. T4. (a) Batchelor dissipation ϵ , (b) gradient Richardson number Ri , (c) Thorpe scale L_T , (d) buoyancy flux $b = gw'\rho'/\rho_0$, (e) north-south component of shear production $-w'u'\partial U/\partial z$, (f) west-east component of shear production $-w'v'\partial V/\partial z$, (g) turbulent Froude number $Fr_t = q/L_T N$ with $q = (w'^2 + u'^2 + v'^2)^{1/2}$, (h) turbulent Reynolds number $Re_t = qL_T/\nu$, and (i) strain ratio $Fr_\gamma = (\epsilon/\nu N^2)^{1/2}$.

turbulence intensity varied greatly in the data set, with the rate of dissipation ϵ ranging from 10^{-10} to 10^{-5} $m^2 s^{-3}$ (Fig. 6). The intermittency factor, σ_{in}^2 (Baker and Gibson 1987), was 2.7, which was close to that observed in the ocean (Baker and Gibson 1987; Gibson 1991). Figure 12 shows the distribution of the strain ratio Fr_γ , where we can see the

variability in the interplay between the inertia, buoyancy, and viscosity in the behavior of the turbulence. Approximately 40% of the turbulent segments (14% of the metalimnion by combining results from Figs. 11 and 12) had Fr_γ higher than 5, the threshold normally assumed to be necessary for sustaining turbulent mixing (Gibson 1980; Rohr et

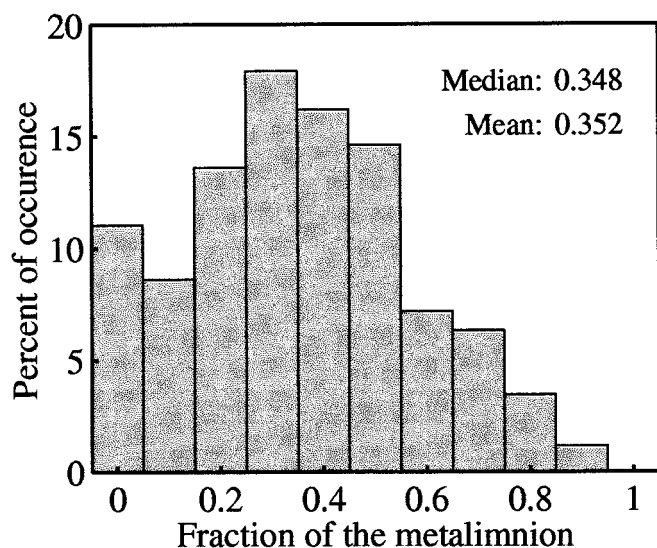


Fig. 11. Histogram of the fraction of the length of the metalimnion covered by turbulent patches. The turbulent patches were defined as statistically stationary segments of the profile with good Batchelor fitting and rate of dissipation $\epsilon > 10^{-10} \text{ m}^2 \text{ s}^{-3}$. The length of the metalimnion was determined by visual inspection of each profile. All the data collected in the 1997, 1998, and 1999 experiments are included in the figure.

al. 1988b). In our case, however, the segments for which Fr_γ was less than 5 still possessed turbulent signatures with good fits to the Batchelor spectrum.

Properties of the turbulence within a turbulent patch

Sparseness and homogeneity of the overturns—Overturns are present whenever the displacement scale L_c is nonzero in any point of the profile. It is to be expected that the more vigorously a turbulent event is mixing the water column, the more uniform the distribution of L_c will be, and the more consistently the overturns fill of the water column will be. One measure of the vigor of the mixing is the strain ratio Fr_γ , which is just the ratio of the rate of strain to the maximum internal wave strain rate. The sparseness of the overturns can be ascertained from the percentage of overturns in each turbulent segment or patch. This is shown in Fig. 13a, where the percentage of overturns increases consistently from 0 to about 55% as Fr_γ increases from <1 to between 5 and 10, after which the data suggest no further decrease in the sparseness (increase in percentage of overturn).

On the other hand, the homogeneity of the overturns may be measured with the skewness of the overturn scale L_c (Teoh et al. 1997). The skewness of the distribution of L_c (Fig. 13b) was essentially positive for all segments (more than 99% of the segments) and, on average, decreased from about 3 to 1 as the strain ratio Fr_γ from 1 to 20. Thus, as Fr_γ increases, more of the segments were filled with overturns and the overturn length scales become more symmetrically distributed. Teoh et al. (1997) were the first to postulate that simple shear driven billows, which occur at low values of gradient Richardson number, are characterized by relatively large displacement scales, large strain ratios,

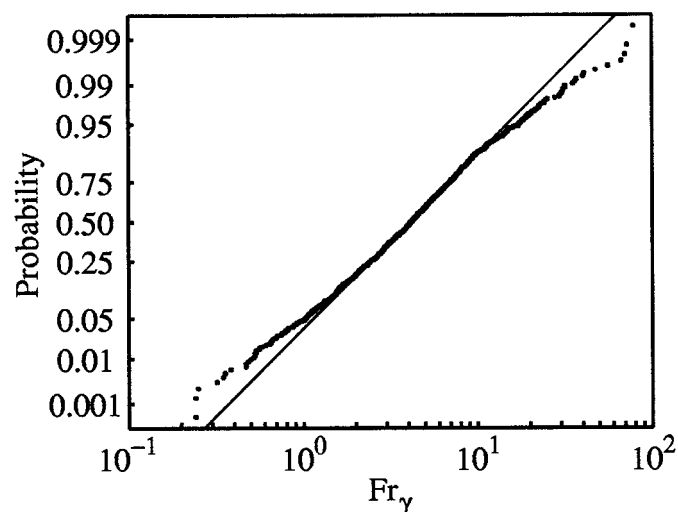


Fig. 12. Probability plot of the strain ratio Fr_γ . Data from the 1997, 1998, and 1999 experiments are plotted together, and the solid line corresponds to the best-fit log-normal distribution. The expected value of Fr_γ is 5.9 with variance of 36.6.

and a balanced symmetric distribution of displacement scales within a segment (small skewness). By contrast, segments that show well-defined turbulent signatures (good Batchelor fits) but have small values of Fr_γ exhibit displacement scale distributions with a larger skewness, which is characteristic of traumata wave-wave interaction (McEwan 1973) that leads to convective instabilities (Teoh et al. 1997).

The high skewness for small strain ratios means that the displacements are made up of a few large overturns within the segment and large sections where the fluid motion was turbulent, but with excursions too small to register as overturns. Such a signature is characteristic of cold (or warm) parcels of fluid being inverted at height (or depth), leading to the development of natural convection. For this reason the algorithm that was used to obtain L_T was modified to calculate the rms of the points with nonzero displacements rather than all the points in the segment.

Isotropy—The ratio between the velocity component fluctuations indicates the degree of isotropy of the turbulence. In Fig. 14a we show that on average the vertical velocity fluctuations were smaller than the horizontal ones at small Fr_γ , indicating the suppression of the vertical motions by the buoyancy. However, as the turbulent events became more energetic and Fr_γ increased, we start to see the ratio w'/q_h increasing to the isotropic value of one and even surpassing this limit in a few data points, as also observed in the ocean (Yamazaki 1990). The observed values larger than one could not be explained, not even by internal wave contamination, since Fr_γ was large. In the horizontal plane we also observed a tendency to isotropy as Fr_γ increases (Fig. 14b). The degree of anisotropy in the horizontal at small Fr_γ can be attributed to the occurrence of horizontal shear distorting the overturns (like in Fig. 9), but we were unable to confirm this hypothesis since we could not decompose the velocity fluctuations along the direction of the shear—despite the shear and Richardson number being basically constant over the segments,

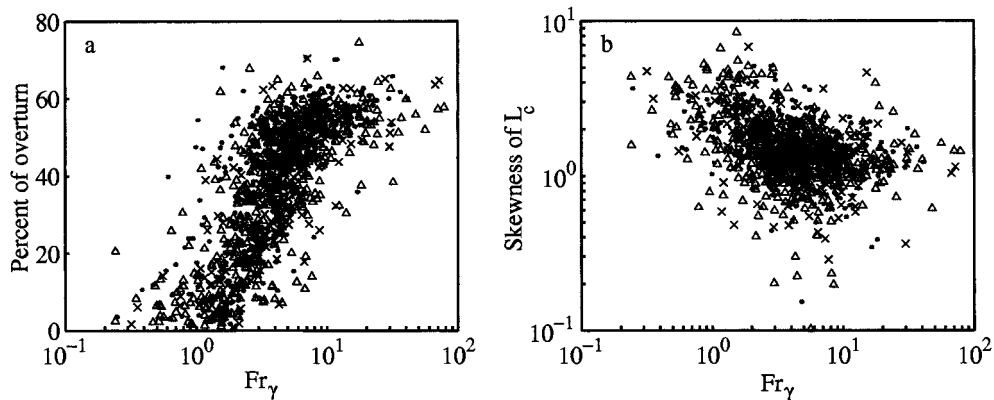


Fig. 13. (a) Percent of overturn and (b) skewness of the centered displacement scale L_c versus the strain ratio Fr_γ , showing that the number of overturns in a turbulent patch increases and becomes more evenly distributed in length scales as the events become more energetic. The percent of overturn was defined as the ratio between the number of samples with $L_c > 0$ in a segment and the total number of samples in that segment. The skewness of the centered displacement scale L_c was defined as $\Sigma(L_{ci} - \bar{L}_{ci})\sigma_{L_c}^{-1}$ over a segment and measures the asymmetry of the distribution of length scales within the segments. The data collected in 1997 are shown as triangles, in 1998 as dots, and in 1999 as crosses.

the direction of the flow was usually changing, making unclear the definition of the direction of the shear at the segment scale. The observed tendency to isotropy at large values of Fr_γ coincides with the laboratory observations of Thoroddsen and Van Atta (1992) and Piccirillo and Van Atta (1997), and with the observations in the ocean of Yamazaki (1990).

Vertical fluxes for mass and momentum—The PFP also allowed the measurement of the vertical fluxes of mass and momentum, enabling us to estimate the net vertical exchange coefficient within the metalimnion.

The buoyancy fluxes were estimated from direct measurements of the velocity and density fluctuations $b_{dm} = \overline{gw'\rho'}/\rho_o$ and by the Osborn–Cox method $b_{OC} = 3\kappa N^2(\partial T'/\partial z)^2/(\partial T/\partial z)^2$, where κ is the molecular diffusion coefficient (Osborn and Cox 1972). In order to compare the direct and indirect

estimates of the fluxes in the metalimnion, we calculate a nondimensional vertical exchange coefficient $bN^{-2}\kappa^{-1}$ (Fig. 15). The physical interpretation of this quantity must be considered with caution due to the presence of down-gradient b_{dm}^+ and up-gradient b_{dm}^- fluxes obtained from the direct measurements (Fig. 15b), as previously observed by Moum (1996a).

The nondimensional vertical exchange coefficient based on both the indirect (Fig. 15a) and the direct (Fig. 15b) estimates of the buoyancy fluxes has a median value around 1 for $Fr_\gamma = 1.7$, a value of 60 for $Fr_\gamma = 6$, and a value of about 10^3 at $Fr_\gamma = 320$. There were a few values with $Fr_\gamma < 1.7$. For these events the contribution due to the turbulent fluctuations is smaller than the molecular diffusivity.

Both the indirect and direct estimates of the exchange coefficient show a similar dependency on Fr_γ , which is an interesting result since b_{OC} is a parameterization of the turbu-

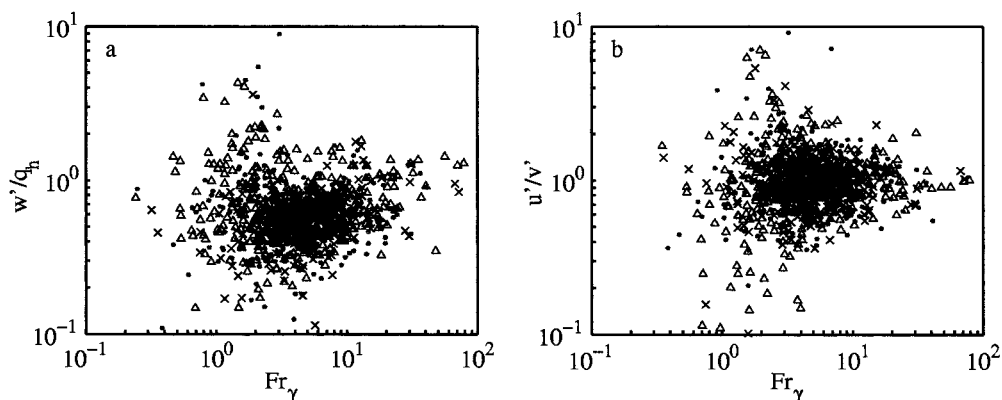


Fig. 14. Strain ratio Fr_γ plotted versus the ratio of rms velocities (a) w'/q_h where $q_h = (u'^2 + v'^2)^{1/2}$ and (b) u'/v' . The horizontal velocity components u' and v' are aligned along the north–south and west–east directions, respectively. The data collected in 1997 are shown as triangles, in 1998 as dots, and in 1999 as crosses.

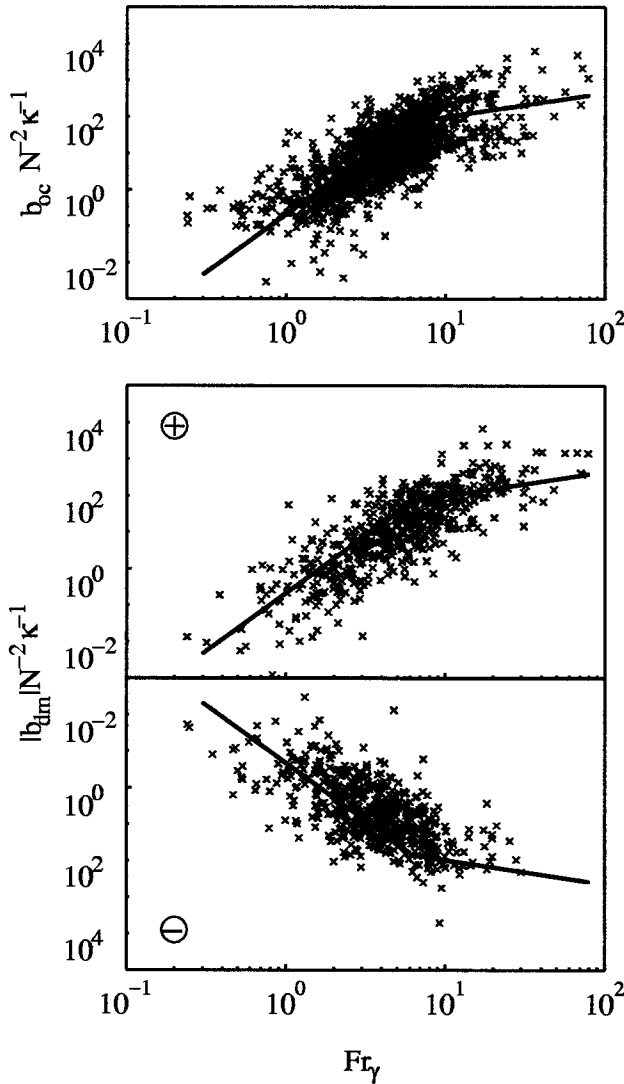


Fig. 15. Nondimensional vertical eddy exchange coefficient $b/(N^2\kappa)$ plotted versus the strain ratio Fr_γ . In (a) b_{OC} correspond to the Osborn–Cox buoyancy flux and in (b) b_{dm} is obtained from direct measurement of the buoyancy flux. Note that in (b) the top panel shows data points with positive buoyancy fluxes and the lower panel shows points with negative fluxes. The lines shown in the plots correspond to $0.21 Fr_\gamma^{19/6}$ for $Fr_\gamma \leq 6$ and $21 Fr_\gamma^{2/3}$ for $6 < Fr_\gamma \leq 100$. The data collected in 1997, 1998, and 1999 are shown in the plots.

lent heat flux, whereas b_{dm} is a measurement of the instantaneous advective fluxes (Winters and D’Asaro 1996). Also observed in Fig. 15b is that $b_{dm}^+ N^{-2} \kappa^{-1}$ reaches higher absolute values than $b_{dm}^- N^{-2} \kappa^{-1}$, and the down-gradient fluxes become more frequent for values of Fr_γ greater than about 6 (Fig. 16). These results agree with the theoretical arguments of Gibson (1980) and the experimental results of Rohr et al. (1988b), who showed turbulence sustaining an irreversible buoyancy flux for strain ratios greater than 5.

Likewise, a nondimensional vertical exchange coefficient for the momentum $[-\overline{w'u'}(\partial U/\partial z)^{-1} - \overline{w'v'}(\partial V/\partial z)^{-1}]\nu^{-1}$ was computed (Fig. 17), which, besides the larger scatter, shows

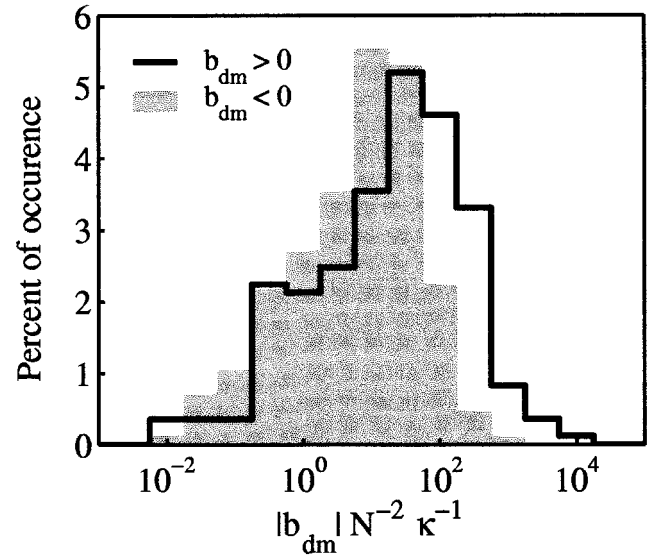


Fig. 16. Histogram of the nondimensional vertical exchange coefficient of mass obtained from direct measurements (Fig. 15b). The histogram of the positive values of the exchange coefficient is under the solid line, and the histogram of the absolute values of the negative measurements is marked with the shading.

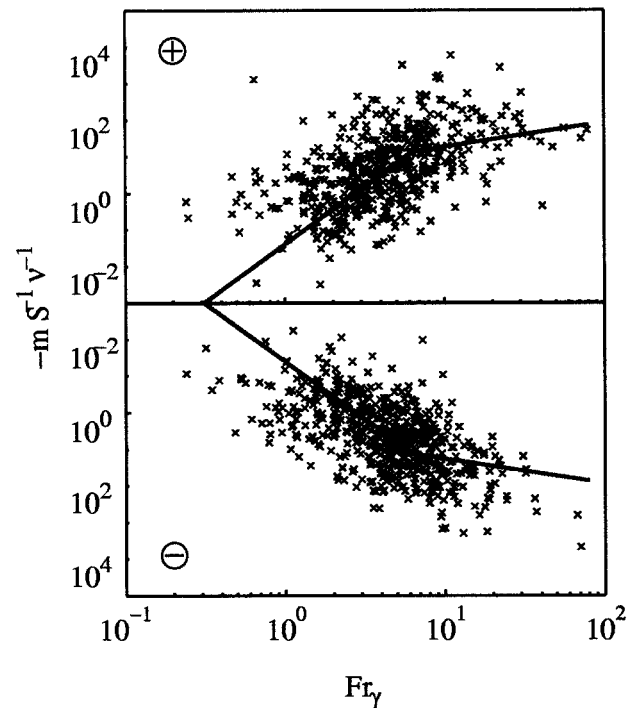


Fig. 17. Nondimensional vertical eddy exchange coefficient of momentum plotted versus the strain ratio. The variable m corresponds to the momentum fluxes $\overline{u'w'}$ and $\overline{v'w'}$ and S is either $\partial U/\partial z$ or $\partial V/\partial z$. In both panels the line for $Fr_\gamma \leq 6$ corresponds to $0.04 Fr_\gamma^{19/6}$ and for $6 < Fr_\gamma \leq 100$ corresponds to $4 Fr_\gamma^{2/3}$.

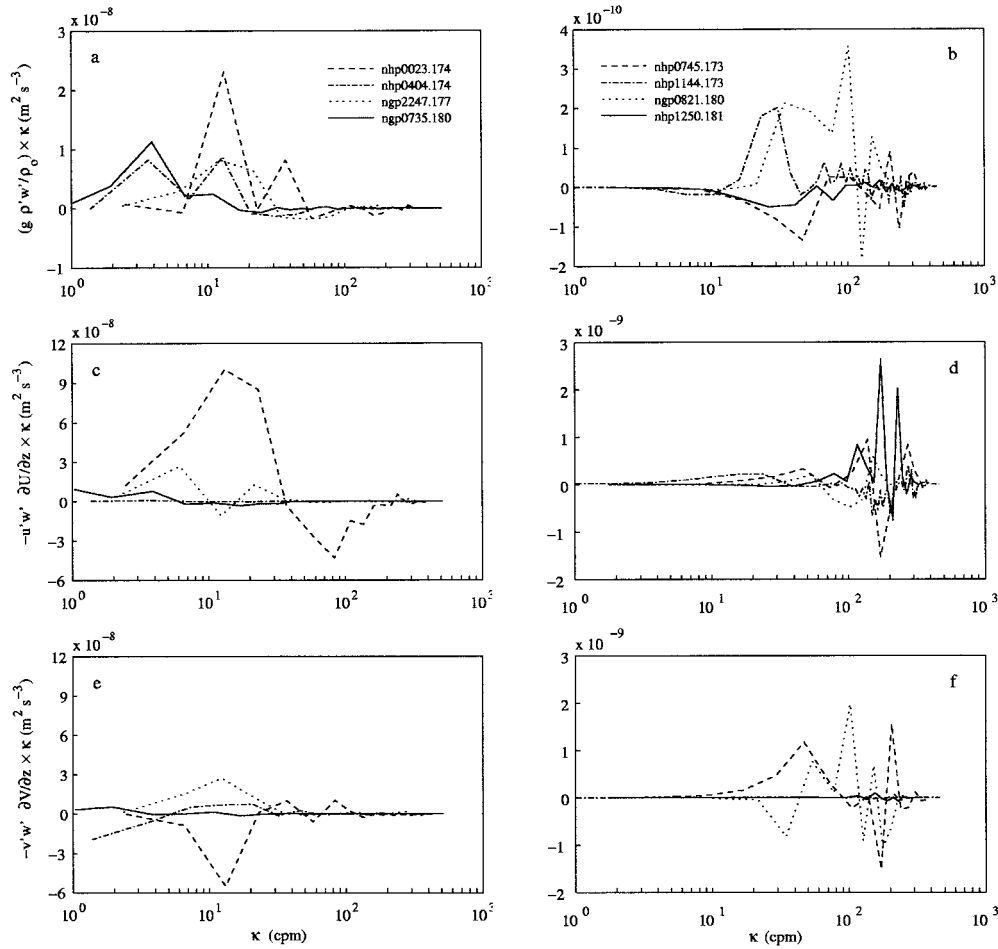


Fig. 18. Cospectra of the buoyancy and momentum flux over (a), (c), (e) segments with $10 < Fr_\gamma < 30$ and $10^{-8} < b_{OC} < 10^{-7} \text{ m}^2 \text{ s}^{-3}$ and (b), (d), (f) segments with $1 < Fr_\gamma < 3$ and $10^{-10} < b_{OC} < 10^{-9} \text{ m}^2 \text{ s}^{-3}$. These segments correspond to points laying at the centered of the distribution of b_{OC} along the Fr_γ axes on Fig. 15. The plots (a), (b) correspond to the buoyancy fluxes, (c), (d) to the momentum flux in the north–south direction, and (e), (f) the momentum flux in the west–east direction. The different lines in the (a), (c), (e) plots correspond to the profiles indicated in the legend in (a), whereas the lines in (b), (d), (f) correspond to the profiles indicated in (b). In the legends, the first three letters discriminate the probe that was used in the profile, the next four digits indicate the time of the profiling, and the last three digits correspond to the Julian day in 1997.

a similar trend with increasing absolute values as Fr_γ increases. The maximum value of the dimensionless exchange coefficient of momentum is about the same as the one obtained for mass (10^3), and a contribution equivalent to molecular transport is again reached at a value of Fr_γ around 1.7.

Figures 15 and 17 show a dependency on Fr_γ , indicating that larger strain ratios result in larger displacement scales and vertical fluxes. The cospectra of the buoyancy and momentum fluxes in Fig. 18 confirm this, showing that the main contribution to the turbulent fluxes at high strain ratio comes from the larger overturns (around 10 cm), whereas the contributions at small strain ratios are smaller and come from the very small overturns (around 2 cm).

Scaling of the turbulence properties

With the PFP we were able to measure temperature, conductivity, and velocity profiles from scales of about 1 mm

to the depth of the water body. As discussed in the previous sections, we have separated mean and internal wave signatures in the flow variables from the turbulence-induced fluctuations by low passing the data through a variable filter with a length proportional to the overturn scale. Properties of the turbulence were then determined by spectral analysis and statistics of the patches in the metalimnion. These results, presented in the last section, suggest the existence of two classes of turbulent regimes: one weak and fine grained, characteristic of internal wave–wave interaction, and the other more energetic and probably due to shear-driven turbulence. In this section we introduce scaling arguments and data fit to further explore the nature of the turbulence in the metalimnion and, also, try to relate direct measurements only available through the PFP with variables more easily obtained (i.e., background shear, stratification, and rate of dissipation).

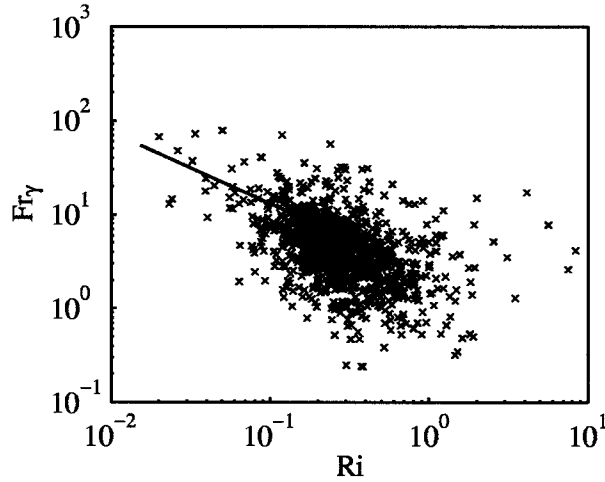


Fig. 19. Gradient Richardson number Ri versus the strain ratio Fr_γ for the data collected in the 1997, 1998, and 1999 field experiments. The line for $Ri \leq 0.25$ corresponds to $2.3Ri^{-3/4}$.

In essentially all laboratory experiments the turbulence is generated by some type of grid arrangement. In numerical work (Jacobitz et al. 1997), an initial disturbance is introduced and then its growth can be observed. However, in the present field situation the turbulence can only depend on the parameter set (ν, κ, S, N, t) where ν is the kinematic viscosity, κ is the molecular diffusivity of heat, S is the mean shear, N is the buoyancy frequency, and t is the time from the beginning of the initiation of the turbulent patch. The parameters S and N may be assumed constant since the overturn length scale L_T , as discussed in the occurrence of turbulent patches in the metalimnion, was always much smaller than the characteristic length scale of either the shear profile $(\partial U/\partial z)/(\partial^2 U/\partial z^2)$ or the density profile $(\partial \rho/\partial z)/(\partial^2 \rho/\partial z^2)$. The flow characteristics can, thus, depend only on the nondimensional parameters (Pr, Ri, T) , where

$$Pr = \frac{\nu}{\kappa}, \quad (1)$$

$$Ri = \frac{N^2}{S^2}, \quad \text{and} \quad (2)$$

$$T = St. \quad (3)$$

Assuming that the flow variables L_T , q , and ϵ are functions of Pr , Ri , and T allows us to write

$$L_T = f_1(Ri, Fr_\gamma) \quad (4)$$

and

$$q = f_2(Ri, Fr_\gamma), \quad (5)$$

where we have made Ri and Fr_γ the independent variables because T is not available and f_1 and f_2 are two unknown functions.

These are rather complicated relationships involving two independent variables, Fr_γ and Ri . For small Ri (large Fr_γ), Stacey et al. (1999) and Ivey and Imberger (1991) showed that these two variables are related. For the present data, Fig.

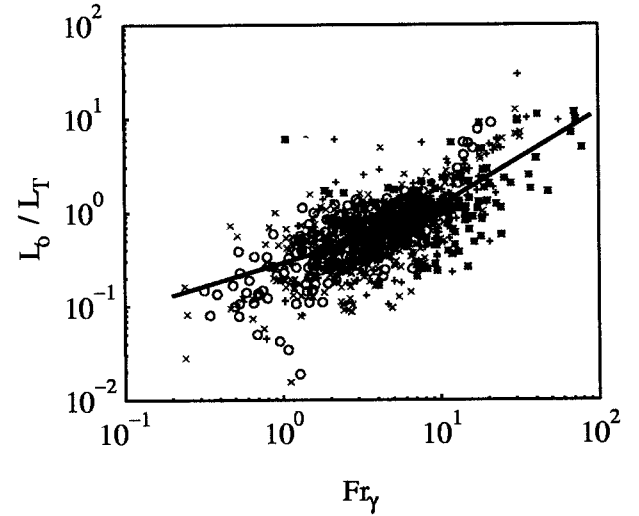


Fig. 20. The strain ratio Fr_γ versus the ratio of length scales L_o/L_T , where L_o is the Ozmidov scale $(\epsilon N^{-3})^{1/2}$ and L_T is the Thorpe displacement scale. The line for $Fr_\gamma \leq 6$ corresponds to $0.29 Fr_\gamma^{1/2}$ and for $6 < Fr_\gamma \leq 100$ corresponds to $0.12 Fr_\gamma$. The data points shown as open circles have $Ri > 0.50$; points shown as crosses have $0.25 < Ri \leq 0.50$, points shown as pluses have $0.15 < Ri \leq 0.25$, and points shown as stars have $0 < Ri \leq 0.15$.

19 also shows a general trend of a decrease of Fr_γ with increasing Ri . However, it is important to observe that the great majority of points lie in the rectangle $(0.1 < Ri < 0.7; 1 < Fr_\gamma < 10)$, implying that the turbulence mixes the density and momentum profiles such that Ri rarely is able to decrease to below 0.1. More data are needed with a greater range of Fr_γ , but for simplicity the dependence of Ri was ignored in the following relationships and discussed again at the end of this section.

The length scale dependence is best revealed by plotting L_o/L_T as shown in Fig. 20. The data are well described by

$$\frac{L_o}{L_T} = 0.29 Fr_\gamma^{1/2} \quad \text{for } Fr_\gamma \leq 6, \quad (6.a)$$

$$\frac{L_o}{L_T} = 0.12 Fr_\gamma \quad \text{for } Fr_\gamma > 6, \quad (6.b)$$

or, as shown in Table 1,

$$\frac{L_T}{L_p} = 3.4 Fr_\gamma^{1/2} \quad \text{for } Fr_\gamma \leq 6, \quad (7.a)$$

$$\frac{L_T}{L_p} = 8.3 \quad \text{for } Fr_\gamma > 6, \quad (7.b)$$

where L_o is the Ozmidov length scale $(\epsilon N^{-3})^{1/2}$ and L_p is the primitive length scale $(\nu N^{-1})^{1/2}$ (Imberger 1994).

The two estimates (Eqs. 7a and 7b) converge at $Fr_\gamma \approx 6$, indicating a transition of processes, also manifested in the skewness and the frequency distributions of the displacement scales (Fig. 13). As mentioned in the previous section, the mass mixing coefficient is equal to 60 times molecular at this value of Fr_γ ; a value of Fr_γ of around 5 is normally associated with the inception of turbulent mixing (Rohr et

Table 1. Turbulence properties.

Quantity	Symbol*	Origin	Small Fr_γ	Large Fr_γ
Overturn length scale	L_T/L_p	Data fit	$3.4Fr_\gamma^{1/2}$	8.3
	L_o/L_T		$0.29Fr_\gamma^{1/2}$	$0.12Fr_\gamma$
Velocity scale	q/q_p	Data fit	$0.5Fr_\gamma^{5/3}$	$3Fr_\gamma^{2/3}$
Reynolds number	$Re_i = qL_T/\nu$	Derived	$1.7Fr_\gamma^{13/6}$	$25Fr_\gamma^{2/3}$
Froude number	$Fr_i = q/NL_T$	Derived	$0.15Fr_\gamma^{7/6}$	$0.36Fr_\gamma^{2/3}$
Taylor scaling	$q(\epsilon L_T)^{-1/3}$	Derived	$0.33Fr_\gamma^{5/6}$	1.5
Mass correlation coefficient	b/N^2L_Tq	Derived	$0.02Fr_\gamma$	0.12
Mass mixing coefficient	$b/\kappa N^2$	Data fit	$0.21Fr_\gamma^{19/6}$	$21Fr_\gamma^{2/3}$
Momentum mixing coefficient	$\frac{u'w'}{v'w'}\nu^{-1}S_x^{-1}$	Data fit	$0.04Fr_\gamma^{9/6}$	$4Fr_\gamma^{2/3}$
	$\frac{v'w'}{v'w'}\nu^{-1}S_y^{-1}$			

* $q_p, (\nu N)^{1/2}; L_p, \nu^{1/2}N^{-1/2}; q_o, \epsilon^{1/2}N^{-1/2}; L_o, \epsilon^{1/2}N^{-3/2}$.

al. 1988b; Itsweire et al. 1993). It should be noted that for our observed high range of strain ratio ($6 < Fr_\gamma \leq 100$) the Grasshof number $Gr_i = N^2L_T^4\nu^{-2}$ of the turbulence was constant ($Gr_i = 0.5 \times 10^9$, from Eq. 7b). The above information, together with the observation of low Ri (Fig. 19) and well-balanced distribution of the displacement scales in the patches (Fig. 13), is consistent with the hypothesis of shear-driven turbulence for the high range of Fr_γ . The field data, however, also clearly showed that for values of Fr_γ between about 1 and 6 there is fine-grained active turbulence mixing that, for its features, is probably due to traumata characteristic of internal wave-wave interaction (Teoh et al. 1997).

Next we considered the variation of the velocity scale that is shown in Fig. 21. Once again good fits were possible with a transition at $Fr_\gamma \approx 6$. Both Figs. 20 and 21 show that the variations of the variables were independent of Ri, but clearly small values of Ri were reflected in the larger Fr_γ values (Fig. 19). The data suggest

$$\frac{q}{q_p} = 0.5Fr_\gamma^{5/3} \quad \text{for } Fr_\gamma \leq 6, \quad (8.a)$$

$$\frac{q}{q_p} = 3Fr_\gamma^{2/3} \quad \text{for } Fr_\gamma > 6. \quad (8.b)$$

From these relationships (Eqs. 7 and 8) follow scales for the Reynolds (Table 1, Fig. 22a), the Froude number Fr_i (Table 1, Fig. 22b), and the Taylor scaling hypothesis parameter $q\epsilon^{-1/3}L_T^{-1/3}$ (Table 1, Fig. 22c). As expected, since these are quantities derived from Eqs. 7 and 8, the fits are generally very good (Fig. 22).

Our observations cover only the range $0.1 < Fr_\gamma \leq 100$ range, apparently short, but the data set is very large and so represents usual conditions in lakes. The turbulence measurements of Yamazaki (1990), Peters et al. (1995a), and Moum (1996b) in the stratified ocean show a similar range but with most of the data lying in $10 < Fr_\gamma < 100$. This difference in the distribution of Fr_γ is in part attributed to differences in the data processing, with these papers giving emphasis to the most energetic patches, but could also be due to their instrument traversing the water column at higher velocities preventing the regime of low Fr_γ from being detected. A comparison between our scaling and their results for the common Fr_γ range is complicated due to different definitions of length and velocity scales adopted; however, the general trend of the Re_i versus the Fr_γ relation (Fig. 22a in this paper and Figs. 8, 9a, and 6 in the above papers, respectively) was comparable with their data showing a slope close to 1 for the high range of Fr_γ (comparable with our derived slope of $2/3$ for $6 < Fr_\gamma \leq 100$).

The correlation coefficient between the density and the velocity is shown in Fig. 23. A large degree of scatter and a high degree of uncertainty exist. However, in the buoyancy and momentum fluxes (Figs. 15 and 17) the scatter is much less. A good fit to the data in Figs. 15 and 17 is given by

$$\frac{b}{\kappa N^2} = 0.21Fr_\gamma^{19/6} \quad \text{for } Fr_\gamma \leq 6, \quad (9.a)$$

$$\frac{b}{\kappa N^2} = 21Fr_\gamma^{2/3} \quad \text{for } Fr_\gamma > 6, \quad (9.b)$$

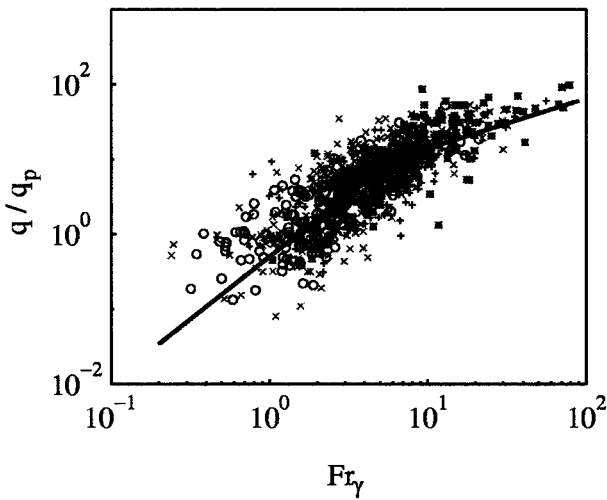


Fig. 21. The strain ratio Fr_γ versus the ratio of velocity scales q/q_p , where q is the velocity scale $(w'^2 + u'^2 + v'^2)^{1/2}$ and q_p is the primitive velocity scale $(\nu N)^{1/2}$. The line for $Fr_\gamma \leq 6$ corresponds to $0.5 Fr_\gamma^{5/3}$ and for $6 < Fr_\gamma \leq 100$ corresponds to $3Fr_\gamma^{2/3}$. The data points shown as open circles have $Ri \geq 0.50$, points shown as crosses have $0.25 < Ri \leq 0.50$, points shown as pluses have $0.15 < Ri \leq 0.25$, and points shown as stairs have $0 < Ri \leq 0.15$.

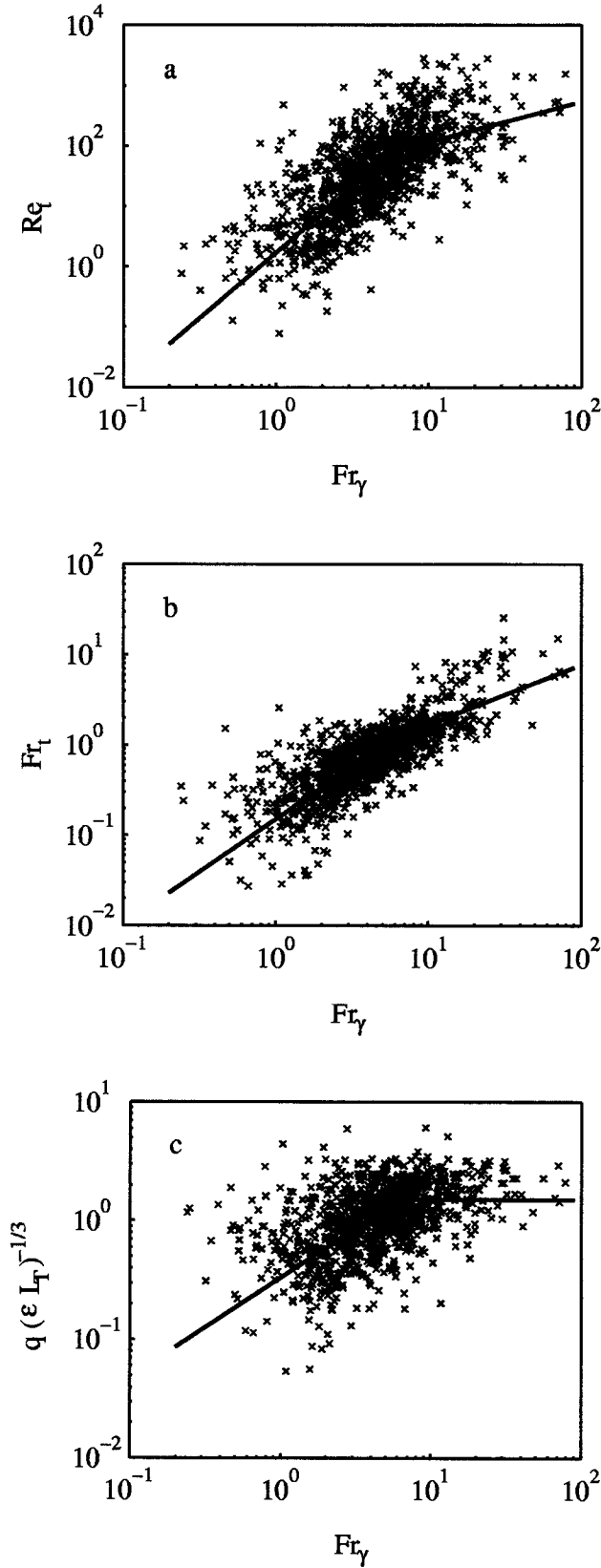


Fig. 22. The strain ratio Fr_γ versus (a) the Reynolds number, (b) the Froude number, and (c) Taylor scaling hypothesis parameter. In (a) the line for $Fr_\gamma \leq 6$ corresponds to $1.7 Fr_\gamma^{1/6}$ and for $6 < Fr_\gamma \leq 100$ corresponds to $25 Fr_\gamma^{2/3}$; in (b) the line for $Fr_\gamma \leq 6$ corre-

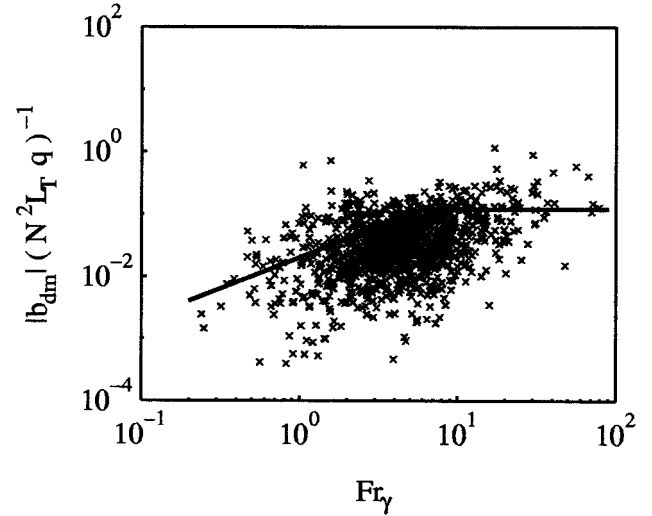


Fig. 23. The correlation coefficient between the buoyancy flux and the scaling $qL_T N^2$ plotted versus the strain ratio Fr_γ . The line shown in the plot for $Fr_\gamma \leq 6$ corresponds to $0.02 Fr_\gamma$ and for $6 < Fr_\gamma \leq 100$ corresponds to 0.12.

$$\frac{m}{\nu S^2} = 0.04 Fr_\gamma^{19/6} \quad \text{for } Fr_\gamma \leq 6, \quad (10.a)$$

$$\frac{m}{\nu S^2} = 4.0 Fr_\gamma^{2/3} \quad \text{for } Fr_\gamma > 6. \quad (10.b)$$

From Eq. 9 follow the relationships for the correlation coefficient shown in Fig. 23 (momentum correlation was similar and is not shown). The fit is representative of the data and is slightly biased toward the larger estimates.

The consistency of the correlation coefficient for large Fr_γ was noted before by Ivey and Imberger (1991), but their analysis of laboratory data indicated a somewhat higher value of 0.3. More data are required to sharpen the value of this constant correlation coefficient.

Given Eqs. 9b and 10b it is possible to define the mixing efficiency R_f if it is assumed for $Fr_\gamma > 6$, corresponding to shear driven turbulence:

$$\kappa_p = \frac{b}{N^2} = 21 Fr_\gamma^{2/3} \kappa, \quad (11.a)$$

$$\kappa_m = \frac{m}{S^2} = 4.0 Fr_\gamma^{2/3} \nu, \quad (11.b)$$

where the symbols have their usual meaning. Energy conservation requires (Ivey and Imberger 1991)

$$m = b + \epsilon. \quad (12)$$

From the definitions it follows directly that

←

sponds to $0.15 Fr_\gamma^{7/6}$ and for $6 < Fr_\gamma \leq 100$ corresponds to $0.36 Fr_\gamma^{2/3}$; and in (c) The line for $Fr_\gamma \leq 6$ corresponds to $0.33 Fr_\gamma^{5/6}$ and for $6 < Fr_\gamma \leq 100$ corresponds to 1.5.

$$R_f = \frac{b}{m} = \frac{\kappa_\rho}{\kappa_m} \text{Ri}. \quad (13)$$

Substituting from Eq. 11 yields

$$R_f = \frac{21}{4} \frac{\text{Ri}}{\text{Pr}}. \quad (14)$$

The maximum value occurs at the largest values of Ri for this high range of strain ratio; thus, $\text{Fr}_\gamma \approx 6$, which corresponds to a value of $\text{Ri} \approx 0.25$ (Fig. 19), leading to $R_f = 0.19$. This is close to the value generally accepted from laboratory experiments (see Ivey and Imberger 1991 for a review).

Equation 11a provides an estimate of the vertical flux in terms of the turbulent kinetic energy dissipation ϵ . If we use the fact that during a mixing event sustained by shear ($\text{Ri} \leq 0.25$) the available kinetic energy is given by $L^3 S^2/12$ (Imberger 1994), then the dissipation that keeps pace with the available kinetic energy at a rate S is given by $L^2 S^3/12$. Substituting for L (large Fr_γ) from Table 1 yields the estimates

$$\text{Fr}_\gamma = \frac{2.3}{\text{Ri}^{3/4}} \quad \text{and} \quad (15)$$

$$\kappa_\rho = \frac{36.6}{\text{Ri}^{1/2}} \kappa \quad (16)$$

for $\text{Ri} \leq 0.25$. The transition given by stability theory ($\text{Ri} = 0.25$) provides a boundary at $\text{Fr}_\gamma = 6.5$ that is very close to the observations. The relationship (Eq. 15) is shown in Fig. 19 and again is in excellent agreement with the observations.

Conclusions

The intensive work in Lake Kinneret for 3 consecutive years, during periods of strong stratification and severe wind forcing, resulted in a large and consistent data set covering a strain ratio's range of $0.1 < \text{Fr}_\gamma \leq 100$, typical for most stratified lakes and oceanic conditions.

The effectiveness of the turbulent displacement scale L_c was tested as a scale for separation of the turbulent fluctuations from the internal wave signal (Peters et al. 1995a). This separation was done by way of a variable filter applied to the measured signals and by integration of spectral properties of the turbulent patches in a range limited by displacement scale.

The sampling in several stations around the lake with the PFP, accompanied by the continuous record of the temperature fluctuations by thermistor chains, showed that the mean flow in the lake was defined by a basin scale internal wave field. It was observed that, despite being vigorous, the internal wave field evolved slowly relative to S^{-1} , resulting in pseudo-steady conditions for the turbulence. The gradient Richardson number associated with this mean shear often decreased to values less than 0.25 but rarely below 0.1.

The turbulence in the lake was intermittent but, on average, 35% of the metalimnion was covered by well-defined turbulent patches during the sampling period. From these

well-defined turbulent patches, only about 40% had $\text{Fr}_\gamma > 6$ and appreciable vertical fluxes ($\kappa_\rho > 10^{-5} \text{ m}^2 \text{ s}^{-1}$). These figures mean that most of the metalimnion had an eddy diffusivity close to the molecular value and only about 14% of its thickness had significant vertical mixing.

The direct measurements of the vertical fluxes obtained from the velocity signals given by the PFP became consistently positive for $\text{Fr}_\gamma > 10$ and, for the observed high values of Fr_γ ($6 < \text{Fr}_\gamma < 100$), the direct measurements were well approximated by the indirect estimates of the vertical fluxes (Osborn and Cox 1972) based on temperature microstructure, most easily measured. From the observations we can also say that as Fr_γ increased the number of overturns within the turbulent patches increased, the turbulence tended toward isotropic conditions, the overturn scales became more uniformly distributed within a segment, and the main contributions to the fluxes changed from small scales to large scales of about 10 cm. For large Fr_γ the down-gradient contributions generally began to overwhelm the up-gradient contributions. Together, this evidence suggests that for small Fr_γ , values generally accepted to contain no turbulent signals, there was active fine-grained turbulence sustained by internal wave-wave traumata as first described by McEwan (1973). Beyond a critical value of Fr_γ of around 6 the turbulent length scales became more uniformly distributed over the segments with overturn scales as large as 10 cm. Since larger values of Fr_γ were consistently associated with values of the gradient Richardson number of less than 0.2, this turbulence was shear driven and is similar to that observed in the ocean and in laboratory experiments. Lack of instrument resolution appears to have prevented the lower Fr_γ range turbulence from being detected in the ocean. Scaling of properties of the turbulence based on Fr_γ and Ri confirmed that there existed two classes of turbulence: one at small Fr_γ and probably energized by wave-wave interactions, and another at large Fr_γ and small Ri, which is shear-driven. This picture was consistent with the observations of the distribution of the displacement scales within the segments (reduction of the skewness and the sparseness in the distributions).

References

- ANTENUCCI, J., J. IMBERGER, AND A. SAGGIO. 2000. Seasonal evolution of the basin-scale internal wave field in a stratified lake. *Limnol. Oceanogr.* **45**: 1621–1638.
- BAKER, M. A., AND C. H. GIBSON. 1987. Sampling turbulence in the stratified ocean: Statistical consequences of strong intermittency. *J. Phys. Oceanogr.* **17**: 1817–1836.
- FOZDAR, F. M., G. PARKER, AND J. IMBERGER. 1985. Matching temperature and conductivity sensor response characteristics. *J. Phys. Oceanogr.* **15**: 1557–1569.
- GARGETT, A. E., AND J. N. MOUM. 1995. Mixing efficiencies in turbulent tidal fronts: Results from direct and indirect measurements of density flux. *J. Phys. Oceanogr.* **25**: 2583–2608.
- GIBSON, C. H. 1980. Fossil temperature, salinity, and vorticity turbulence in the ocean, p. 221–257. *In* *Marine turbulence*. Elsevier.
- . 1991. Turbulence, mixing, and heat flux in the ocean main thermocline. *J. Geophys. Res.* **96**: 20403–20420.
- GLOOR, M., A. WÜEST, AND M. MÜNNICH. 1994. Benthic boundary mixing and resuspension induced by internal seiches. *Hydrobiologia* **284**: 59–68.

- HENDRICKS, P. J., AND G. RODENBUSCH. 1981. Interpretation of velocity profiles measured by freely sinking probes. *Deep-Sea Res.* **28A**: 1199–1213.
- IMBERGER, J. 1994. Transport processes in lakes: A review, p. 99–193. *In* R. Margalef [ed.], *Limnology now: A paradigm of planetary problems*. Elsevier.
- . 1998. Flux paths in a stratified lake: A review, p. 1–18. *In* J. Imberger [ed.], *Physical processes in lakes and oceans*. Coastal and Estuarine Studies. AGU.
- , AND B. BOASHASH. 1986. Application of the Wigner-Ville distribution to temperature gradient microstructure: A new technique to study small-scale variations. *J. Phys. Oceanogr.* **12**: 1997–2012.
- , AND R. HEAD. 1994. Measurement of turbulent properties in a natural system. *In* *Fundamental and Advancements in Hydraulic Measurements and Experimentation*. Hydraulics Division/ASCE.
- , AND G. N. IVEY. 1991. On the nature of turbulence in a stratified fluid. Part II: Application to lakes. *J. Phys. Oceanogr.* **21**: 659–679.
- ITSWEIRE, E. C., J. KOSEFF, D. BRIGGS, AND J. FERZIGER. 1993. Turbulence in stratified shear flows: Implications for interpreting shear-induced mixing in the ocean. *J. Phys. Oceanogr.* **23**: 1508–1522.
- IVEY, G., AND J. IMBERGER. 1991. On the nature of turbulence in a stratified fluid. Part I: The energetics of mixing. *J. Phys. Oceanogr.* **21**: 650–658.
- JACOBITZ, F. G., S. SARKAR, AND C. W. VAN ATTA. 1997. Direct numerical simulations of the turbulence evolution in a uniformly sheared and stably stratified flow. *J. Fluid Mech.* **342**: 231–261.
- LEMCKERT, C., AND J. IMBERGER. 1998. Turbulent benthic boundary layer mixing events in fresh water lakes, p. 481–494. *In* J. Imberger [ed.], *Physical processes in lakes and oceans*. Coastal and Estuarine Studies. AGU.
- LUKETINA, D. A. 1987. Frontogenesis of freshwater overflows. Ph.D. thesis, Univ. Western Australia.
- , AND J. IMBERGER. 2000. Determining turbulent kinetic energy dissipation from Batchelor curve fitting. *J. Atmos. Ocean. Technol.*, In press.
- MCEWAN, A. D. 1973. Interactions between internal gravity waves and their traumatic effect on a continuous stratification. *Boundary-Layer Met.* **5**: 159–175.
- MOUM, J. N. 1990. The quest for k_p —preliminary results from direct measurements of turbulent fluxes in the ocean. *J. Phys. Oceanogr.* **20**: 1980–1984.
- . 1996a. Efficiency of mixing in the main thermocline. *J. Geophys. Res.* **101**: 12,057–12,069.
- . 1996b. Energy containing scales of turbulence in the ocean thermocline. *J. Geophys. Res.* **101**: 14,095–14,109.
- MÜNNICH, M., A. WÜEST, AND D. M. IMBODEN. 1992. Observations of the second vertical mode of the internal seiche in an alpine lake. *Limnol. Oceanogr.* **37**: 1705–1719.
- NISHRI, A., AND OTHERS. 2000. The physical regime and the respective biogeochemical processes in Lake Kinneret lower water mass. *Limnol. Oceanogr.* **45**: 972–981.
- OSBORN, T. R. 1980. Estimates of the local rate of vertical diffusion from dissipation measurements. *J. Phys. Oceanogr.* **10**: 83–89.
- , AND C. S. COX. 1972. Oceanic fine structure. *Geophys. Fluid Dyn.* **3**: 321–345.
- PETERS, H., M. C. GREGG, AND T. B. SANFORD. 1994. The diurnal cycle of the upper equatorial ocean: Turbulence, fine-scale shear and mean shear. *J. Geophys. Res.* **99**: 7707–7723.
- , ———, AND ———. 1995a. Detail and scaling of turbulent overturns in the Pacific Equatorial undercurrent. *J. Geophys. Res.* **100**: 18349–18368.
- , ———, AND ———. 1995b. On the parameterization of equatorial turbulence: Effect of fine-scale variations below the range of the diurnal cycle. *J. Geophys. Res.* **100 (C9)**: 18,333–18,348.
- PICCIRILLO, P. 1993. An experimental study of the evolution of turbulence in a uniformly sheared thermally stratified flow. Ph.D. thesis, Univ. California, San Diego.
- , AND C. W. VAN ATTA. 1997. The evolution of a uniformly sheared thermally stratified turbulent flow. *J. Fluid Mech.* **334**: 61–86.
- ROHR, J. J., E. C. ITSWEIRE, K. N. HELLAND, AND C. W. VAN ATTA. 1988a. An investigation of the growth of turbulence in a uniform mean shear flow. *J. Fluid Mech.* **187**: 1–33.
- , ———, ———, AND ———. 1988b. Growth and decay of turbulence in a stably stratified shear flow. *J. Fluid Mech.* **195**: 77–111.
- STACEY, M. T., S. G. MONISMITH, AND J. R. BURAU. 1999. Observations of turbulence in a partially stratified estuary. *J. Phys. Oceanogr.* **29**: 1950–1970.
- TEOH, S. G., G. N. IVEY, AND J. IMBERGER. 1997. Laboratory study of the interactions between two internal wave rays. *J. Fluid Mech.* **336**: 91–122.
- THORODDSEN, S. T., AND C. W. VAN ATTA. 1992. The influence of stable stratification on small-scale anisotropy and dissipation in turbulence. *J. Geophys. Res.* **97**: 3647–3658.
- THORPE, S. A. 1977. Turbulence and mixing in a Scottish loch. *Philos. Trans. R. Soc. Lond., A* **286**: 125–181.
- WINTERS, K. B., AND E. A. D'ASARO. 1996. Diascalar flux and the rate of fluid mixing. *J. Fluid Mech.* **317**: 179–193.
- YAMAZAKI, H. 1990. Stratified turbulence near a critical dissipation. *J. Phys. Oceanogr.* **20**: 1583–1598.
- , AND T. OSBORN. 1993. Direct estimation of heat flux in a seasonal thermocline. *J. Phys. Oceanogr.* **23**: 503–516.

Received: 14 December 1998

Accepted: 9 August 2000

Amended: 10 October 2000